



RESEARCH ARTICLE

10.1029/2025MS005104

Key Points:

- Ocean simulations with partially resolved boundary layer turbulence exhibit resolution-dependent sensitivity to choice of turbulence closure
- In the gray zone resolutions, $k-\epsilon$ can accurately represent mean-state properties but excessively damp small-scale turbulence
- Using Smagorinsky or the implicit method in the gray zone allows active turbulence despite sacrificing mean state fidelity

Supporting Information:

Supporting Information may be found in the online version of this article.

Correspondence to:

Z. Chen,
zchen43@umd.edu

Citation:

Chen, Z., Wenegrat, J., Chor, T., & Marchesiello, P. (2025). Evaluating turbulence parameterizations at gray zone resolutions for the ocean surface boundary layer. *Journal of Advances in Modeling Earth Systems*, 17, e2025MS005104.
<https://doi.org/10.1029/2025MS005104>

Received 1 APR 2025

Accepted 9 SEP 2025

Evaluating Turbulence Parameterizations at Gray Zone Resolutions for the Ocean Surface Boundary Layer

Zihan Chen¹ , Jacob Wenegrat¹ , Tomás Chor¹, and Patrick Marchesiello² 

¹Department of Atmospheric and Oceanic Science, University of Maryland-College Park, College Park, MD, USA,

²Université de Toulouse, LEGOS (CNES/CNRS/IRD/UPS), Toulouse, France

Abstract Turbulent mixing in ocean boundary layers is often fully parameterized as a subgrid-scale process in realistic ocean simulations. However, recent submesoscale modeling studies have advanced to a horizontal grid spacing of $\mathcal{O}(10\text{ m})$ that is comparable to, or even smaller than, the typical depth of the turbulent surface boundary layer. Meanwhile, efforts toward realistic large-eddy simulations (LES) nested within regional models require subdomains with similar grid spacings, where turbulent eddies are partially resolved in the mixed layer. The range of intermediate grid spacings, often known as the “gray zone,” presents challenges for model configuration and analysis, including uncertainties regarding the behavior of common turbulence closures outside of their ideal use cases. In this study, we evaluate three common configurations for subgrid turbulence — $k-\epsilon$, Smagorinsky, and an implicit no-closure method—in the gray zone resolutions for the ocean surface mixed layer. Results indicate that, in the gray zone with partially resolved boundary layer turbulence, $k-\epsilon$ can produce accurate mixed layer profiles with little sensitivity to grid spacing. However, it overly damps turbulent motions, significantly reducing small-scale variability that could otherwise be captured. The Smagorinsky closure and the implicit method, in contrast, exhibit higher sensitivity to grid spacing, initially performing poorly but converging toward baseline solutions at finer grids. Our findings provide guidance for submesoscale and turbulent-scale modeling, recommending Smagorinsky or implicit methods for nested domains which prioritize resolved turbulence, such as LES. The $k-\epsilon$ closure is suitable for simulations that aim to achieve accurate mean-state representations rather than explicitly resolving detailed three-dimensional turbulence.

Plain Language Summary Turbulence is an important small-scale process that mixes heat, momentum, and nutrients near the ocean surface and bottom. Typically, ocean models cannot fully resolve turbulent motions due to limited grid resolution and instead rely on parameterizations to approximate the effects of turbulent mixing. However, as regional models improve and begin to resolve boundary layer turbulence at finer resolutions, choosing appropriate parameterizations becomes increasingly important. Here, we evaluate three common model approaches for subgrid turbulence closure across the intermediate resolution known as the “gray zone,” where critical processes of boundary layer turbulence are only partially represented by the model grid. The $k-\epsilon$ closure accurately represents boundary mixing regardless of resolution but suppresses smaller-scale turbulence. In contrast, the Smagorinsky closure and the implicit method are sensitive to resolution, performing poorly at coarse grids but substantially improving at higher resolutions. Our findings suggest using Smagorinsky or implicit methods for simulations aimed at explicitly resolving turbulent motions (e.g., nested large eddy simulations), while the $k-\epsilon$ closure is better suited for scenarios prioritizing accurate mean conditions over detailed turbulence features.

1. Introduction

Realistic regional ocean simulations now regularly resolve submesoscale eddies at a grid spacing of $\mathcal{O}(1\text{ km})$ (Gula et al., 2021; Taylor & Thompson, 2023). Through multiple nesting steps, many studies have also successfully further refined the model grid spacing to $\mathcal{O}(10\text{ m})$ to investigate mixed-layer processes, such as Langmuir circulation (Hypolite et al., 2022), symmetric instability (Dong et al., 2022), and submesoscale shelf currents (Dauhajre et al., 2019). Relative to the typical value of mixed layer depth at $\mathcal{O}(100\text{ m})$, realistic simulations at horizontal grid spacings of $\mathcal{O}(10\text{ m})$ can represent, albeit coarsely, large turbulent eddies in the mixed layer. However, despite being turbulence-permitting, these simulations generally employ vertical mixing parameterizations designed for global and regional ocean simulations, for example, the K-profile parameterization (KPP, Large et al., 1994) and the $k-\epsilon$ model (Jones & Launder, 1972), the latter of which is derived from the Reynolds-averaged Navier-Stokes (RANS) equations framework. In RANS closures such as $k-\epsilon$, mixing is

parameterized by assuming that all boundary-layer turbulence is unresolved. This assumption is violated when the turbulent eddies start to be resolved at a finer model grid, which leads to concerns of double counting turbulence from directly resolved eddies and subgrid processes, both in terms of energetics and effects on dynamics.

Ideally, the emergence of boundary layer turbulent eddies requires a shift of modeling paradigm from RANS to large-eddy simulation (LES), where most eddies are explicitly resolved and only the small eddies are parameterized for the subgrid mixing effect (e.g., Smagorinsky-Lilly model, see Lilly, 1962). In practice, however, the grid spacing of $\mathcal{O}(10\text{ m})$ for ocean surface boundary layer is still too coarse to be in the inertial subrange for the LES closure to appropriately represent the energy cascade. This dilemma posed by the lack of scale separation at intermediate grid resolutions is commonly known as the “gray zone” problem, first introduced in the atmospheric sciences literature (Wyngaard, 2004), but with relatively little work to-date specifically for ocean modeling. In this study, we aim to characterize the gray zone issues of classical RANS and LES turbulence closures in the context of the ocean surface boundary layer, with the goal to inform modeling strategies and guide development of scale-aware parameterizations.

Representing turbulent flows at the gray zone resolution has been a subject of extensive research for atmospheric modeling (F. Chow et al., 2019; Honnert et al., 2020). For example, Zhou et al. (2014) performed simulations for the atmospheric convective boundary layer and found that the use of a one-dimensional planetary boundary layer parameterization in gray zone resolution resulted in overly large convection cells and a delayed onset of turbulence. The gray zone issue also often appears in model nesting applications, where a high-resolution grid is embedded within a coarser parent grid that provides the lateral boundary conditions required to accurately simulate fine-scale flow within a limited area. For instance, Mirocha et al. (2013) and Goodfriend et al. (2015) noted that the choice of subgrid closure could affect the transition to turbulence at the coarse-fine domain interface. Treatments at the lateral boundaries, such as increasing forcing frequency (Brisson et al., 2016), adding synthetic perturbations (Mazzaro et al., 2017), and optimizing grid aspect ratios (Daniels et al., 2016), have shown to improve turbulence spin-up in the inner domain. For atmospheric modeling, the gray zone problem has led to the active development of many scale-aware turbulence parameterizations (F. K. Chow et al., 2005; Bhattacharya & Stevens, 2016; Kurowski & Teixeira, 2018), which enable the transition from the bulk representation of the planetary boundary layer to three-dimensional turbulence. For ocean modeling, it is desirable to apply scale-aware turbulence parameterizations, but very few studies have implemented or tested these in the ocean context (cf. Ilcak et al., 2008). To date, most ocean models (e.g., ROMS, CROCO, and MITgcm) do not support scale-aware parameterizations.

For ocean modeling, the gray zone problem has already been a practical concern and will become more prevalent in the future. Our study thus aims to evaluate RANS and LES turbulence closures ($k-\epsilon$, Smagorinsky, and the implicit method) in the gray zone resolutions that allow the partial representation of boundary layer turbulence. Here, we orient our analysis to two common modeling scenarios that may face the gray zone problem. First, for stand-alone submesoscale-resolving simulations—where the objective is to well resolve processes at $\mathcal{O}(100\text{ m})$ —we focus on the representation of averaged mixed layer profiles and the evolution of mixed layer depth. Second, for a nested LES within a regional domain—where the objective is the best possible representation of turbulence statistics as the gray zone is traversed with telescoping resolution grids—we evaluate the representation of turbulent coherent structures, fluxes, and kinetic energy. In the following sections, we first define the problem setup and numerical simulations in Section 2. Section 3 describes the results and makes recommendations based on the modeling objectives. Finally, results are summarized in Section 4, along with a discussion of the limitations and future research directions.

2. Methods

2.1. Model Description

The Coastal and Regional Ocean Community model, CROCO Version 1.3.0 (Auclair et al., 2022), is used to simulate turbulence in the upper ocean boundary layer. In this study, we broadly define the gray zone as a range of horizontal grid spacings extending from the scale of mixed layer depth to well-resolved LES, for which turbulent eddies are allowed to appear (coarsely resolved) in the mixed layer (further details on grid spacing can be found in Section 2.2). The same non-hydrostatic, non-Boussinesq solver is applied to all simulations with the fifth-order weighted essentially non-oscillatory (WENO5) scheme for both momentum and tracer advection. This setup follows CROCO's documentation on LES applications by Jullien et al. (2022) as well as the best practices

according to Pressel et al. (2017). Recently, CROCO's non-hydrostatic solver and the WENO5 scheme have been compared to the US National Center for Atmospheric Research's LES model (NCAR-LES) and demonstrated good accuracy for surface boundary layer turbulence problems (Fan et al., 2023), however, as noted below in some cases implicit diffusion appears to play a significant role relative to explicit diffusion, such that higher-order schemes would be preferable. We have also tested non-diffusive advective schemes but found inferior model solutions relative to WENO5 (see Supporting Information S1 for details).

Two turbulence closures in CROCO, the k - ϵ model (Jones & Launder, 1972) and the Smagorinsky-Lilly model (Lilly, 1962), are evaluated for their performance in the gray zone. While KPP is another common closure for ocean modeling, it underperformed in our preliminary tests relative to two-equation models like k - ϵ for the gray zone where turbulent eddies are partially resolved. Therefore, we limit our scope to k - ϵ as the representative RANS closure in this study. As an additional point of comparison, we run simulations without an explicit turbulence closure: an alternative approach relying instead on the dissipative nature of the quasi-monotonic advection scheme (WENO5) to provide an implicit model of subgrid turbulence. In the LES framework, this is known as implicit LES (ILES, Grinstein et al., 2007), and it has shown good accuracy for turbulent flows in a wide range of atmospheric and oceanic contexts (Pressel et al., 2017; Silvestri et al., 2024; Smolarkiewicz et al., 2007). Readers should note that implementations of the closures used here may vary across different models and it is often possible to further optimize closure performance by targeted re-tuning for specific forcing regimes (Umlauf & Burchard, 2005; Wagner et al., 2025). However, while parameter tuning is an important step for model development (Wagner et al., 2025), the ad hoc approach is unlikely to generalize for the gray zone both because a ground truth (i.e., lab measurement or high-fidelity LES) is often unavailable and because of the computational expense of optimizing parameters in very high-resolution realistic simulations. Hence, we do not include such efforts here (see Section 4 for discussion of scale-aware parameterizations).

The k - ϵ model is a common RANS closure used for ocean modeling, for example, in the basin-scale submesoscale-permitting simulations of the Atlantic Ocean (GIGATL) (Gula et al., 2021) and the idealized simulations of ice dynamics in the surface mixed layer (Herman et al., 2020). In CROCO, k - ϵ is implemented as part of the Generic Length Scale mixing parameterization (Umlauf & Burchard, 2003), which solves the transport equations for turbulent kinetic energy (TKE, k) and its dissipation rate (ϵ) to compute eddy viscosity, K_{gls} . As a vertical mixing parameterization in CROCO, the shear production term for TKE, $P = K_{gls} \left[(\partial_z u)^2 + (\partial_z v)^2 \right]$ accounts only for the vertical shear of the horizontal velocity rather than the full deformation rate. Meanwhile, the advection terms in the total derivatives of k and ϵ include both horizontal and vertical components. The eddy viscosity and diffusivity are computed with the stability function from Canuto et al. (2001). The minimum TKE parameter is set to $10^{-10} \text{ m}^2 \text{ s}^{-2}$ while the background viscosity and diffusivity are prescribed as a constant $10^{-6} \text{ m}^2 \text{ s}^{-1}$. Note that the formulation of k - ϵ in CROCO v1.3.0 does not take into account the Stokes drift and considers the Eulerian shear alone.

Similar to the wide applicability of k - ϵ , the Smagorinsky model is a common closure in the LES framework where comparatively large 3D turbulent eddies are explicitly resolved while smaller-scale motions are modeled. Typically, LES requires the grid configuration to be fine enough to resolve at least 80% of the energy in turbulent motions (Pope, 2000). For optimal performance, the filter width should be placed within the inertial subrange to ensure a proper representation of the energy cascade. In CROCO, the Smagorinsky model follows the formulation by Lilly (1962) to calculate eddy viscosity but separates the horizontal and vertical directions, namely

$$K_{smag} = \begin{cases} C_s^2 \Delta_x \Delta_y D & \text{(horizontal),} \\ C_s^2 \Delta_z^2 D & \text{(vertical)} \end{cases} \quad (1)$$

where $D = \sqrt{2S_{ij}S_{ij}}$ and $S_{ij} = 0.5(\partial_{x_i}u_j + \partial_{x_j}u_i)$ is the strain rate. The Smagorinsky coefficient C_s is fixed at the canonical value of 0.16, and the filter width is taken as the horizontal grid spacings (Δ_x and Δ_y) and the vertical grid spacing (Δ_z). Note that this anisotropic treatment of the eddy viscosity differs from traditional implementations of the Smagorinsky model, which assume isotropic eddy viscosity (Chamecki et al., 2019). Additionally, CROCO applies a buoyancy adjustment such that when a form of the critical Richardson number (N^2/D^2) is larger than 0.25 (strongly stratified regions), the eddy viscosity is set to a constant background value

Table 1

Surface Forcing Conditions for the Five Scenarios Evaluated in the Gray Zone Resolution Using the CROCO Model

Forcing case	F (W m $^{-2}$)	B_s (m 2 s $^{-3}$)	w_* (m s $^{-1}$)	τ_x (N m $^{-2}$)	u_* (m s $^{-1}$)	u_s (m s $^{-1}$)	La_t	Λ
Convection-only	-100	4.87×10^{-8}	1.14×10^{-2}	0	0	0	∞	∞
Shear-only	0	0	0	0.10	9.95×10^{-3}	0	∞	0
Convection-wind	-100	4.87×10^{-8}	1.14×10^{-2}	0.10	9.95×10^{-3}	0	∞	0.61
Wind-wave	0	0	0	0.037	6.05×10^{-3}	6.79×10^{-2}	0.30	0
Convection-wind-wave	-65	3.20×10^{-8}	9.83×10^{-3}	0.037	6.05×10^{-3}	6.79×10^{-2}	0.30	1.76

of 10^{-6} m 2 s $^{-1}$. The turbulent diffusivity is set to K_{smag} with a constant turbulence Prandtl number (Pr) equal to 1. For the Smagorinsky model's typical use in an LES, the grid spacing must be within the inertial subrange, and the grid cells should have a near-unity aspect ratio. Therefore, applying the Smagorinsky model in the gray zone is beyond its intended use case due to insufficient resolution and a large aspect ratio (i.e., horizontal grid spacing is much larger than vertical). Nevertheless, for nested LES, it is often unclear when and how to switch from a RANS closure to a LES closure. To address this, it is necessary to evaluate the Smagorinsky model's performance as part of a down-scaling strategy that nests across the gray zone.

2.2. Simulation Configuration

This study focuses on canonical turbulence regimes relevant to the ocean surface boundary layer, including idealized simulations forced by constant, spatially homogeneous surface buoyancy flux, wind stress, and surface gravity waves in a doubly periodic domain. We note that spatially inhomogeneous mean flows, such as submesoscale fronts, can modify the parameter space of turbulence production and dissipation (Dong et al., 2024; Zheng et al., 2025); however, these cases are left for future work.

A total of five cases are designed to represent different types of turbulent flow (Table 1). To differentiate the relative contribution to turbulence kinetic energy, we map the surface forcings on an La_t , Λ parameter space (Figure 1). The turbulent Langmuir number (La_t) quantifies the competition between the wind-driven shear turbulence and the vortex forcing associated with the Stokes-drift velocity (McWilliams et al., 1997) and is defined as

$$La_t = (u_*/u_s)^{1/2}, \quad (2)$$

where $u_* = (|\tau|/\rho_0)^{1/2}$ is the friction velocity and $u_s = \omega^3 a^2 g^{-1}$ is the surface Stokes drift for deep water waves. The surface forcings for wind drag (τ), wave frequency (ω), and wave amplitude (a) are applied only in the x -direction. The reference density (ρ_0) is chosen to be 1,010 kg m $^{-3}$ (assuming constant salinity) along with a standard value of gravity ($g = 9.81$ m s $^{-2}$).

The stability parameter (Λ) characterizes the relative impacts of wind stress and surface buoyancy fluxes and is defined as

$$\Lambda = \kappa w_*^3/u_*^3, \quad (3)$$

where $\kappa = 0.41$ is the von Kármán constant and $w_* = (B_s|h|)^{1/3}$ is the turbulent convective velocity. The surface buoyancy flux, B_s , is related to the heat flux F by

$$B_s = \frac{\alpha g}{\rho_0 c_p} F, \quad (4)$$

where $\alpha = 2 \times 10^{-4}$ °C $^{-1}$ is the thermal expansion coefficient used in the linear equation of state and $c_p = 3985$ J (kg °C) $^{-1}$ is the specific heat capacity. A boundary layer depth, h , of 30 m (set from the initial condition) is used to calculate w_* , even though the evolution of h varies depending on the surface forcings.

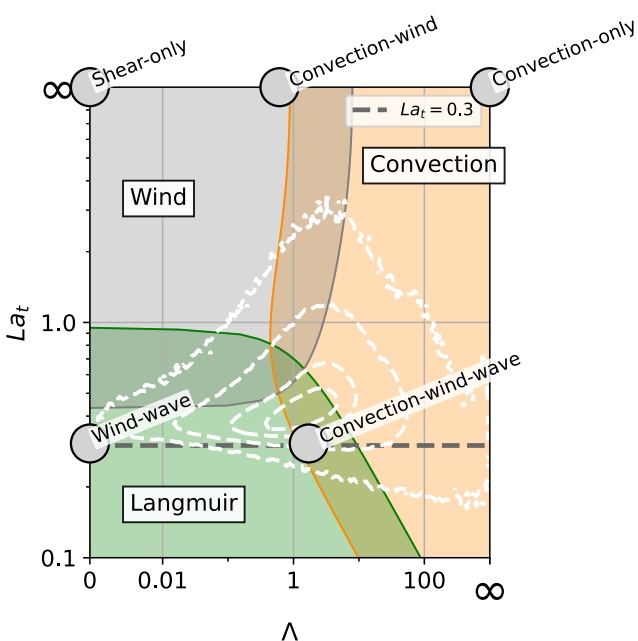


Figure 1. Five forcing cases, shown as gray circles in an La_t - Λ space (see also Chor et al., 2021). The solid blue, gray, and red lines denote regions where more than 25% of the turbulence kinetic energy is produced by Langmuir forcing, wind stress, or buoyancy fluxes, respectively. The dashed white lines represent the joint probability distribution function of the realistic ocean from Li et al. (2019).

the Smagorinsky closure, serving as a well-resolved baseline for comparison (see Supporting Information S1 for a discussion on grid resolution). The computational domain is horizontally periodic, with 256×256 grid points for the 1.25 and 4 m runs and 128×128 for the rest. We have conducted grid convergence tests to verify that the domain size is sufficient for the 1.25 and 4 m runs (see also Supporting Information S1). All runs share the same 100-point vertical grid configuration (using CROCO's grid parameters: $\theta_s = 11.97$, $\theta_b = 0$, $hc = 401.69$, and $h = 131.46$), which maintains an approximately constant 1 m spacing above 60 m depth and gradually stretches to 4 m near the bottom. A sponge layer is applied to the bottom 20 grid points, where the velocity field is nudged to zero and the temperature is relaxed toward the initial stratification. The combination of the stretched vertical grid and sponge layer damps internal waves and minimizes their reflection at the bottom, helping to isolate surface mixing dynamics.

The initial condition for all simulations consists of a resting, stratified ocean. A 30 m mixed layer with a uniform temperature of 20°C is positioned on top of a stratified interior with $N^2 = 1.96 \times 10^{-5} \text{ s}^{-2}$ (equivalent to $0.01^\circ\text{C m}^{-1}$). To accelerate the transition to turbulence in the mixed layer, some small Gaussian noise with a zero mean and a standard deviation of $5 \times 10^{-7}^\circ\text{C}$ is added to the temperature field. All runs are integrated for four inertial periods with a constant Coriolis frequency of 10^{-4} s^{-1} .

The non-hydrostatic solver of CROCO uses a time-splitting method with two user-defined time steps for the fast and slow modes. For the baseline run at $\Delta = 1.25$ m, we use a slow mode time step of 0.5 s and a fast mode time step of 0.017 s, ensuring the Courant number remains below 0.68 for the Courant-Friedrichs-Lowy (CFL) condition. For gray zone runs at coarser grid spacings, longer time steps are used (1 s for slow mode; 0.05 s for fast mode). A wide range of time steps was tested, and these values were selected to balance numerical stability and computation efficiency. To further relax the sound-related CFL constraint, we set the speed of sound $C_s = 3 \text{ m s}^{-1}$ and the second viscosity $\lambda = 10 \text{ kg s}^{-1} \text{ m}^{-1}$ in the fast mode. Despite these non-physical values, Fan et al. (2023) shows that they have minimal impact on turbulence statistics.

To account for the effect of surface gravity waves, the wave-current interaction option was activated in CROCO (MRL_WCI) to use a vortex-force formalism of the primitive equations (Marchesiello et al., 2015; McWilliams et al., 2004; Uchiyama et al., 2010). We prescribe monochromatic wave forcings ($\omega = 1.01 \text{ rad s}^{-1}$ and $a = 0.8 \text{ m}$) to generate a uniform Stokes drift profile aligned with the wind forcing ($\tau_x = 0.037 \text{ N m}^{-2}$), resulting in a wind-wave equilibrium at $La_t = 0.3$ for both the wind-wave and convection-wind-wave cases. The same set of forcings was used in the LES study on Langmuir turbulence by McWilliams et al. (1997) and was revisited with non-hydrostatic CROCO by Herman et al. (2020). The other cases have no wave forcing such that $La_t \rightarrow \infty$. For the stability parameter, we choose $\Lambda = 0.61$ for the convection-wind case to reflect the shear-dominated turbulence generation with a weak convection. In the realistic convection-wind-wave case, $\Lambda = 1.76$ falls between the 60% and 90% contours of the joint probability density function reported by Li et al. (2019), indicating a surface forcing condition representative of the real ocean. The convection-only case has no wind forcing for $\Lambda \rightarrow \infty$ and the shear-only case has no surface buoyancy flux giving $\Lambda = 0$.

Given that the precise definition of the gray zone range remains an area of ongoing research (Beare, 2014; F. Chow et al., 2019; Honnert et al., 2020), we do not attempt to provide a rigorous framing here. Relative to an initial mixed layer depth of 30 m, we choose the horizontal grid spacings to be 4, 12, 24, and 48 m ($\Delta = \Delta_x = \Delta_y$, identical in both the x and y directions). Our post hoc analysis suggests that these grid spacings effectively span the gray zone in our simulations, as indicated by the emergence of turbulent eddies. To evaluate the gray zone results, each forcing case includes a 1.25 m run with

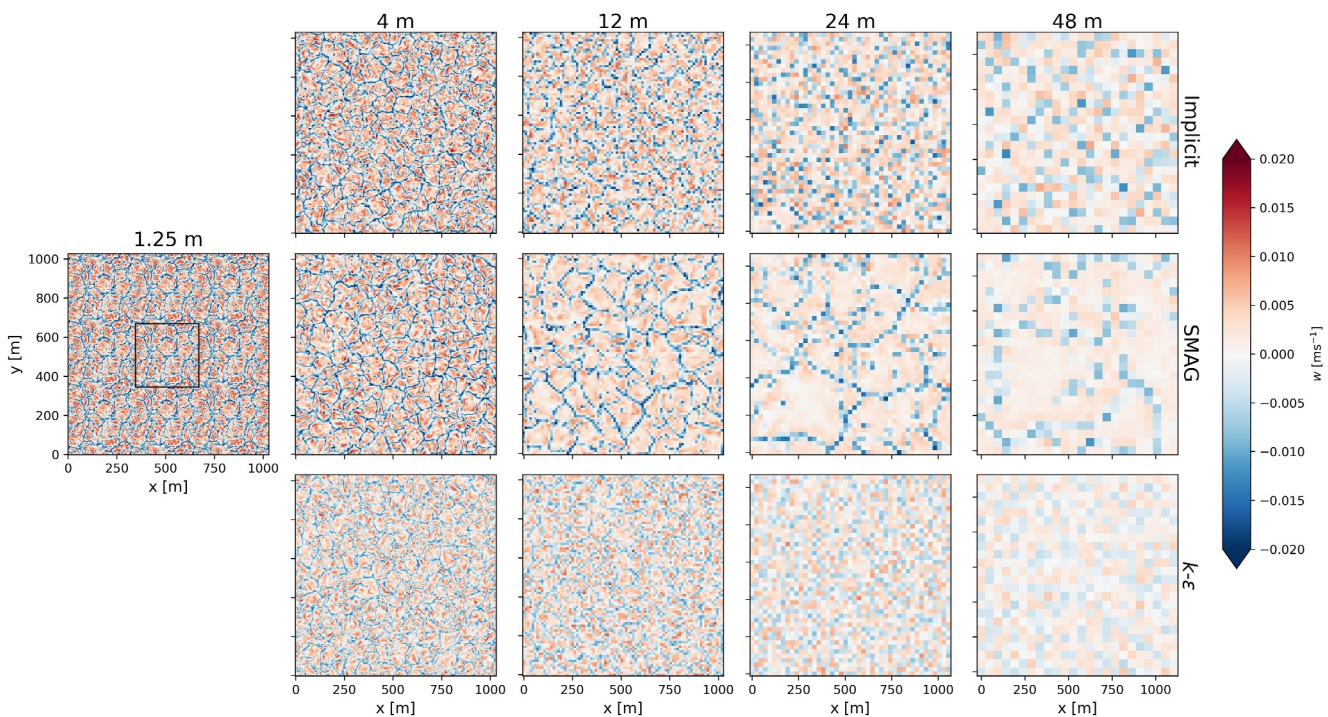


Figure 2. Snapshots of the vertical velocity (w) from the convection-only case at 10 m depth after four inertial periods. Each row is organized to show the results of the same closure at different grid spacings. The 1.25 m Smagorinsky result is tiled periodically to match the domain size of other runs, with the rectangle denoting the original domain.

3. Results

To evaluate closure performance in the gray zone, we first describe the instantaneous coherent turbulence structures under different forcing scenarios (Section 3.1). Next, spatio-temporally averaged mixed-layer profiles (i.e., temperature, velocity, and fluxes of temperature and momentum) are analyzed to quantify the impact of grid spacing on turbulent mixing, followed by a discussion on the evolution of mixed layer depth. Finally, we compare kinetic energy spectra to assess the closure effect on effective resolution.

3.1. Coherent Turbulence Structure

Analyzing flow structures provides a valuable qualitative metric for evaluating marginally resolved eddies in the gray zone. Accurately representing turbulent structures is crucial for nested simulations, as grid-dependent flow artifacts can propagate from the parent domain and contaminate the final solutions (F. Chow et al., 2019). Here, we present coherent turbulence structures as instantaneous flow fields in a horizontal plane near the surface ($z = 10$ m), four inertial periods after the model initialization.

Convection-driven turbulence exhibits characteristic cell-like patterns, which are visible in the high-resolution simulations shown in Figure 2. For example, at $\Delta = 4$ m (MLD $\sim 14 \Delta$), Smagorinsky, $k\text{-}\epsilon$, and implicit runs all display the classic signature of convection cells with strong downwelling boundaries (blue) and broad centers of weak upwelling (red). Driven by surface cooling, the cellular patterns are similar to those found in other simulations of the surface ocean mixed layer (Chor et al., 2018; Souza et al., 2020) and the atmospheric boundary layer heated from below (Honnert et al., 2011; Zhou et al., 2014). At larger grid spacings, the cellular pattern persists at $\Delta = 12$ m but becomes barely visible at $\Delta = 24$ and 48 m. Among the closures, the $k\text{-}\epsilon$ runs produce the weakest vertical velocities, suggesting damping of the resolved turbulence. Meanwhile, in the Smagorinsky runs, the size of the convection cells are resolution-dependent, increasing with the horizontal grid spacing at a rate faster than seen in the implicit case. This behavior may indicate a limitation of the Smagorinsky model in the gray zone, where it struggles to represent subgrid dissipation and impacts kinetic energy across different scales (see Section 3.2.1 for further discussion on subgrid fluxes).

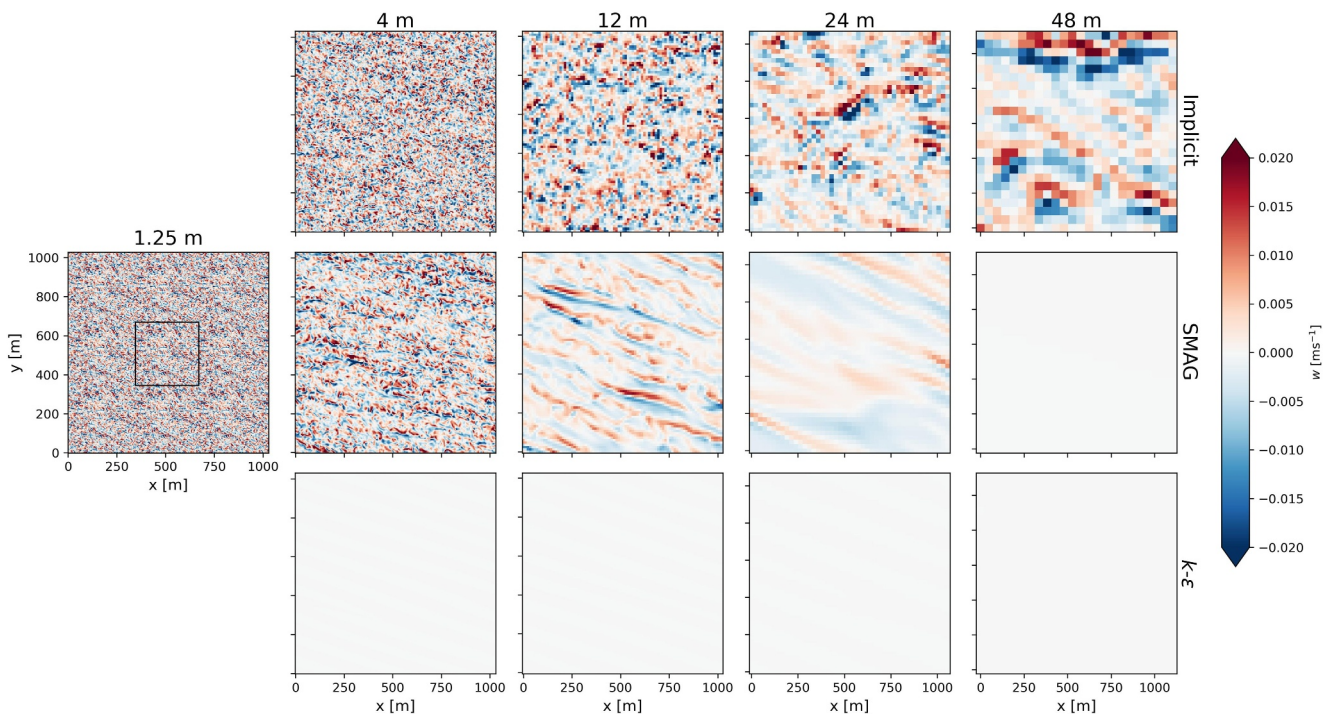


Figure 3. Snapshots of the vertical velocity (w) from the shear-only case at 10 m depth after four inertial periods. Each row is organized to show the results of the same closure at different grid spacings. Note that no turbulence appears in the $k-\epsilon$ runs and the 48 m Smagorinsky run. The 1.25 m Smagorinsky result is tiled periodically to match the domain size of other runs, with the rectangle denoting the original domain.

The shear-driven turbulence case exhibits diverse fine-scale features including streaks and rolls (Figure 3). Unlike convection, the turbulence patterns are highly sensitive to both closure and grid spacing. In particular, $k-\epsilon$ consistently produces a horizontally homogeneous flow field with near-zero vertical velocity regardless of grid spacing. Despite the lack of resolved turbulence, $k-\epsilon$ still drives vertical mixing through subgrid processes, as shown later in the flux profile (Section 3.2.2). For Smagorinsky runs, the turbulence structure changes at different grid spacings. The flow fields display eddies at $\Delta = 4$ m and elongated streaks at $\Delta = 12$ and 24 m. At $\Delta = 48$ m (comparable to the MLD at 40 m), no turbulence appears. The implicit runs exhibit turbulence patterns throughout the gray zone resolutions, but the small scale eddies appear to be more isotropic than the Smagorinsky solutions at similar resolutions. As shown later in Section 3.2.2, although both the Smagorinsky and implicit runs allow turbulence to form, they struggle to generate sufficient vertical mixing to deepen the mixed layer at coarse grid spacings ($\Delta = 24$ and 48 m).

The wind-wave case is designed to generate Langmuir turbulence under strong wind and wave conditions typical of the surface ocean (Belcher et al., 2012). With $La_t = 0.3$, the roll-cell pattern of Langmuir circulations (concentrated horizontal convergence zones and strong downwelling lines) exhibits strong sensitivities to grid spacing and subgrid closures (Figure 4). Unlike the homogeneous flow in the shear-only case, $k-\epsilon$ generates the roll-cell pattern with the additional forcing of Stokes drift. However, compared to Smagorinsky and the implicit method, $k-\epsilon$ produces relatively smooth velocity gradients, again indicating excessive damping of resolved turbulence (as discussed in Section 3.4 when analyzing flow spectra). A parameter recalibration for $k-\epsilon$ may help alleviate the issue of over-damping, but it is beyond the scope of our present work. The relative width of roll cells appears to be sensitive to the grid spacing for both Smagorinsky and the implicit method, increasing from about 100 m at $\Delta = 1.25$ m to over 400 m at $\Delta = 24$ m. In contrast, $k-\epsilon$ shows less sensitivity to grid spacing, consistently producing roll cells with a characteristic width of about 100 m across all grid spacings. At $\Delta = 48$ m, the Smagorinsky solution does not show turbulent eddies, whereas $k-\epsilon$ and the implicit method still generate weak but coherent downwelling lines. This aligns with previous modeling studies by Hypolite et al. (2021, 2022), which reported a similar sensitivity of roll cell width to model resolution in the realistic simulations of the California Current system.

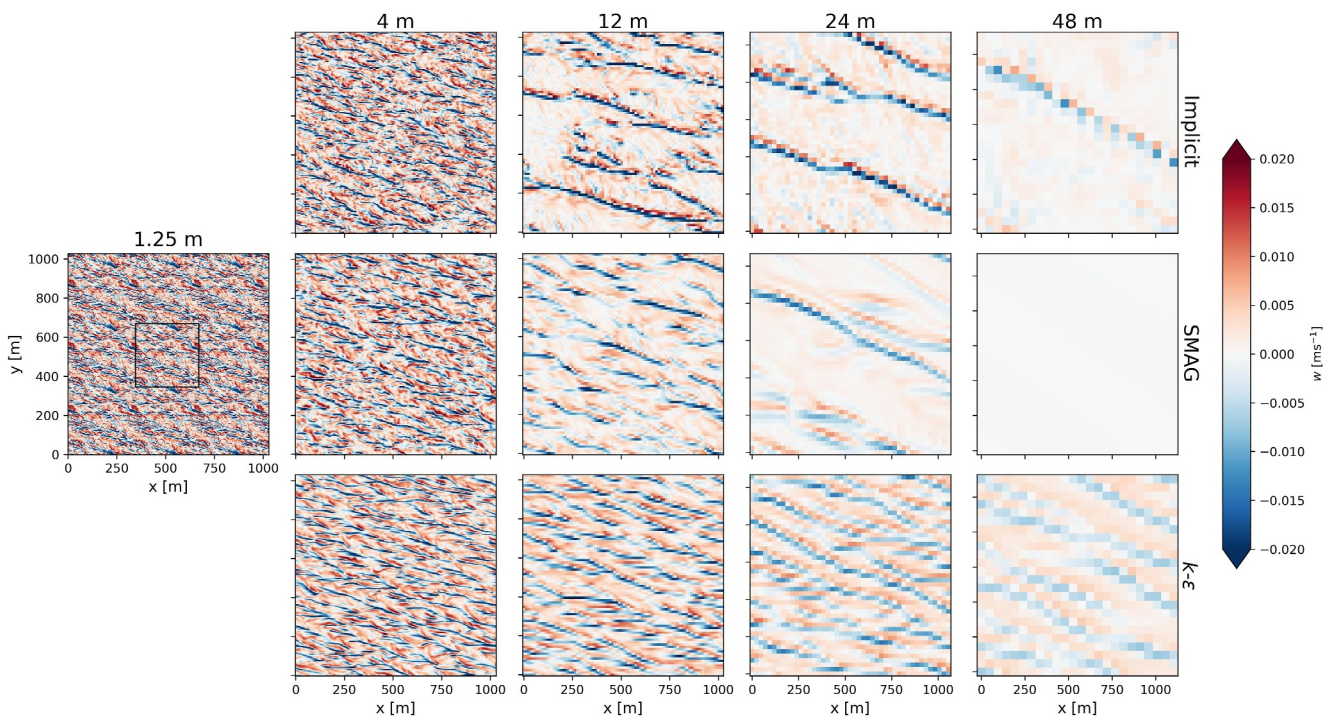


Figure 4. Snapshots of the vertical velocity (w) from the wind-wave case at 10 m depth after four inertial periods. Each row is organized to show the results of the same closure at different grid spacings. Note that no turbulence appears in the 48 m Smagorinsky run. The 1.25 m Smagorinsky result is tiled periodically to match the domain size of other runs, with the rectangle denoting the original domain.

The other forcing cases exhibit similar sensitivities in their coherent structure to closure and grid spacing, with additional figures provided in Supporting Information S1. While this section only offers a qualitative discussion of flow patterns, the representation of coherent turbulence structures has important implications for model nesting in the gray zone. Although increasing the size of the inner domain may help turbulence to spin up once being advected from the parent domain, the inner domain is ultimately constrained by the parent domain size, while a larger domain can also add significant computation cost. In general, the comparison of turbulence structure here shows a pattern of convergence toward the 1.25 m Smagorinsky run as the grid resolution increases, even though in the shear-only case there are some qualitative differences between the implicit and Smagorinsky solutions. We find that $k\text{-}\epsilon$ tends to damp turbulent eddies more than Smagorinsky and the implicit method, with the shear-only case being the most pronounced example (see Supporting Information S1 for a comparison of eddy viscosity simulated by $k\text{-}\epsilon$ and Smagorinsky). When an LES is nested within a regional simulation, excessively laminar flow at the boundary may suppress turbulence development in the inner domain. Compared to $k\text{-}\epsilon$ in the gray zone, using Smagorinsky and the implicit method produces different turbulence patterns, which can propagate into the inner domains and influence the final solutions. In the next section on mixed-layer profiles, we move toward the quantitative evaluation of boundary mixing in the gray zone.

3.2. Mixed Layer Profiles

This section examines the horizontally-averaged properties of the mixed layer—including temperature, velocity, and stratification profiles—for the convection-only (Section 3.2.1), shear-only (Section 3.2.2), and convection-wind-wave cases (Section 3.2.3). Flux profiles are separated into resolved and subgrid components. All profiles are averaged horizontally at each depth and temporally over the last inertial period.

3.2.1. Convection-Only

Figure 5 presents the temperature and stratification profiles (N^2) from the convection-only case. Each panel displays the gray zone profiles of different grid spacings, compared to the baseline solution ($\Delta = 1.25$ m, Smagorinsky) in red. Qualitatively, the averaged profiles under convection-driven turbulence show little

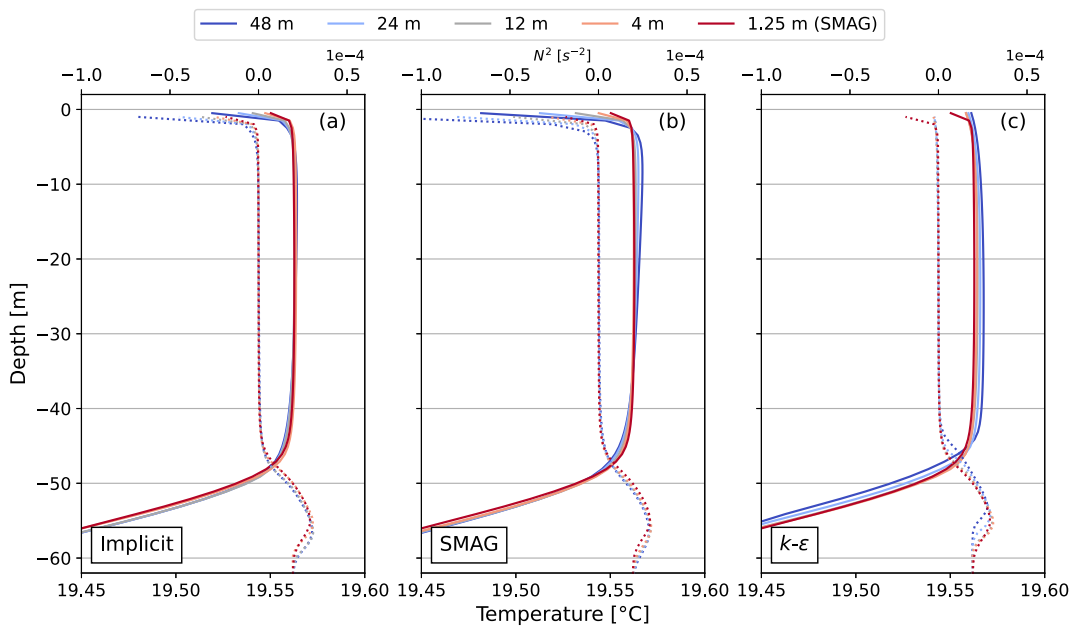


Figure 5. Mean-state temperature (solid lines) and stratification (dotted lines) profiles from the convection case by (a) the implicit method, (b) the Smagorinsky model, and (c) the $k-\epsilon$ model. Along with the temperature profiles (solid lines) in the top panels, the accompanying N^2 profiles are shown as dotted lines. The 1.25 m Smagorinsky run is used as the baseline of comparison (red lines).

sensitivity to changes in grid spacing and closure, relative to other forcing cases below. For the implicit and Smagorinsky solutions, the most notable deviations from the baseline solution occur near the surface above a depth of 5 m. In contrast, the $k-\epsilon$ solutions exhibit greater differences at the bottom of the mixed layer, between 45 and 55 m. A clear convergence of results is observed as the grid spacing is refined.

Figure 6 presents the vertical velocity variance and temperature flux profiles in the convection case. Regardless of closure, the velocity variances increase with smaller grid spacings, corresponding to more active turbulent eddies (Section 3.1). The damping effect of $k-\epsilon$ on resolved turbulence, previously observed in the flow visualization, is also evident here, with the smallest variances relative to those in the Smagorinsky and implicit runs. For temperature fluxes, all runs show similar total flux magnitudes, regardless of closures or grid spacing. This suggests that larger turbulent temperature anomalies at lower resolutions compensate for reduced vertical velocities.

For the temperature profiles of $k-\epsilon$ in Figure 6f, the total fluxes remain consistent despite varying degrees of resolved turbulence at different grid spacings. The relative fraction of subgrid component ($-\bar{K}_s \partial_z T$, where K_s is eddy diffusivity) compensates for changes in the resolved component ($w' T'$). Small differences emerge in the entrainment layer (40–60 m), where the higher-resolution runs produce slightly enhanced negative temperature flux. Previously, Umlauf and Burchard (2005) have also evaluated the performance of $k-\epsilon$ for free convection and reported good approximations of buoyancy flux and entrainment depth. The flux profiles here suggest $k-\epsilon$ is able to predict the total flux profile well (resolved plus subgrid) even with partially resolved turbulence in the gray zone regime that is beyond its typical use case in RANS.

In Figures 6d and 6e, the temperature flux profiles from the Smagorinsky and the implicit runs show striking similarities. The subgrid fluxes by Smagorinsky are negligible, suggesting that numerical dissipation from the advection scheme alone provides most of the diffusion. While this behavior is acceptable from a model fidelity perspective, it is not entirely desirable, as the model effectively functions as an implicit LES despite the prescription of an explicit closure. A higher-order advection scheme (not currently available in CROCO) could potentially mitigate this issue. However, since this behavior is observed only in free convection, it may not be a concern in more realistic configurations (Section 3.2.3).

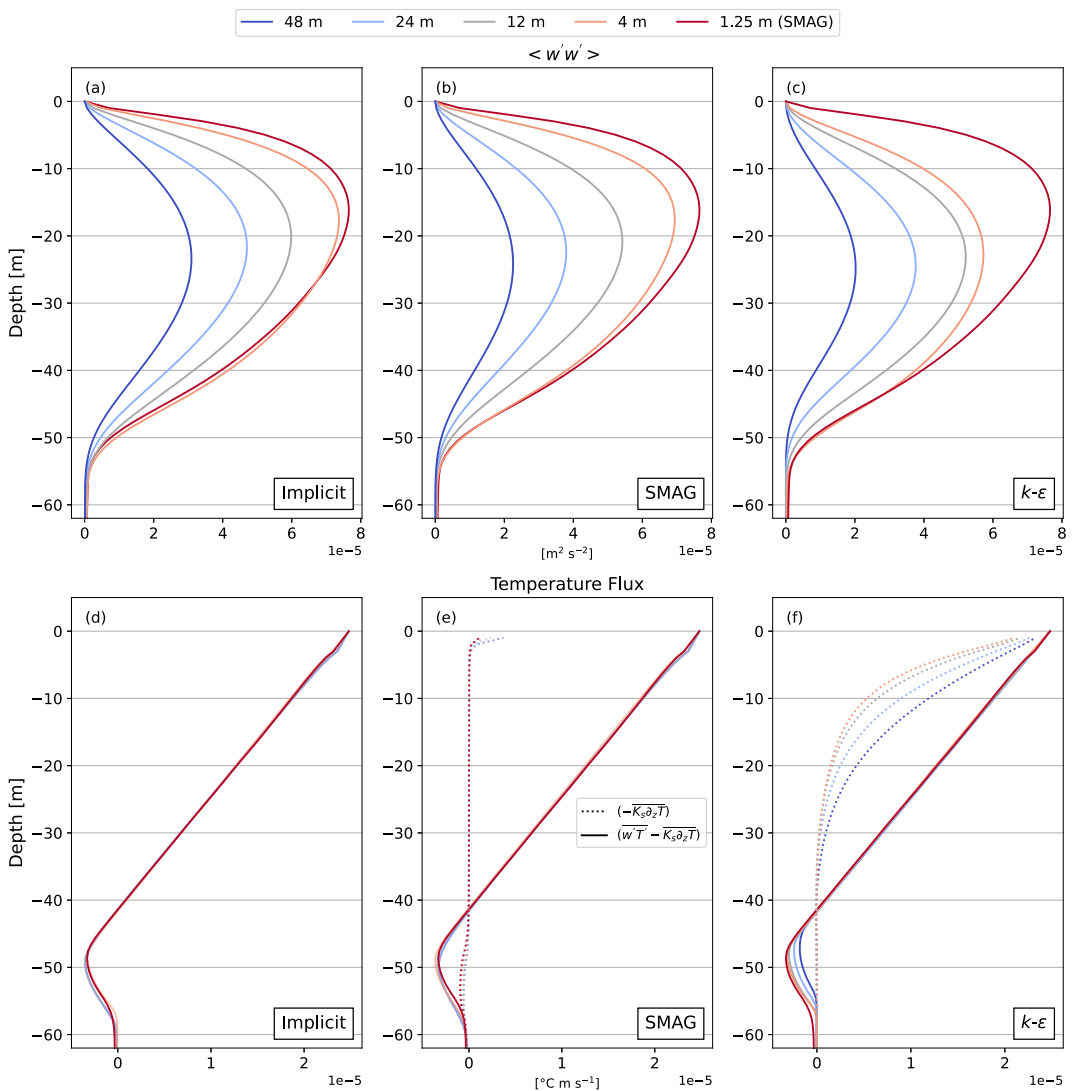


Figure 6. Averaged vertical velocity variance and temperature fluxes in the convection case by the implicit method (a, d), the Smagorinsky model (b, e), and the $k-\epsilon$ model (c, f), where the total flux is denoted as the solid lines and the subgrid component as dotted lines. The 1.25 m Smagorinsky run is used as the baseline of comparison in red lines.

3.2.2. Shear-Only

Compared to free convection, the shear-only case is far more sensitive to closure choice. In the $k-\epsilon$ runs, turbulent mixing is entirely represented by subgrid processes. Figure 7c shows that $k-\epsilon$ produces identical, well-mixed temperature and velocity profiles at different grid spacings, with zero velocity variance (Figure 8c) and only subgrid fluxes ($-\bar{K}_m \partial_z u$ where K_m is eddy viscosity; See Figure 8f). The lack of resolution sensitivity reflects the expected behavior of $k-\epsilon$ as a RANS turbulence closure, which is well validated for free-shear flows. Compared to Smagorinsky and the implicit solutions (Figures 7a and 7b), $k-\epsilon$ generates a deeper mixed layer, with strong stratification in the entrainment layer at 45 m. The maximum N^2 is almost twice as large as the baseline solution (Figure 7c).

The sensitivity to grid spacing is particularly pronounced for Smagorinsky and the implicit method. At $\Delta = 48$ m, the Smagorinsky solution shows no turbulent eddies (Figure 3). The temperature profile remains at 30 m from the initial condition, while the velocity profile shows strong surface shear above 10 m (Figure 7e); At $\Delta = 48$ m, the momentum flux is entirely subgrid above 10 m in response to the surface wind forcing, while the temperature flux is negligible at all depths (Figures 8e and 8h). These profiles suggest that the mixed layer is not being deepened

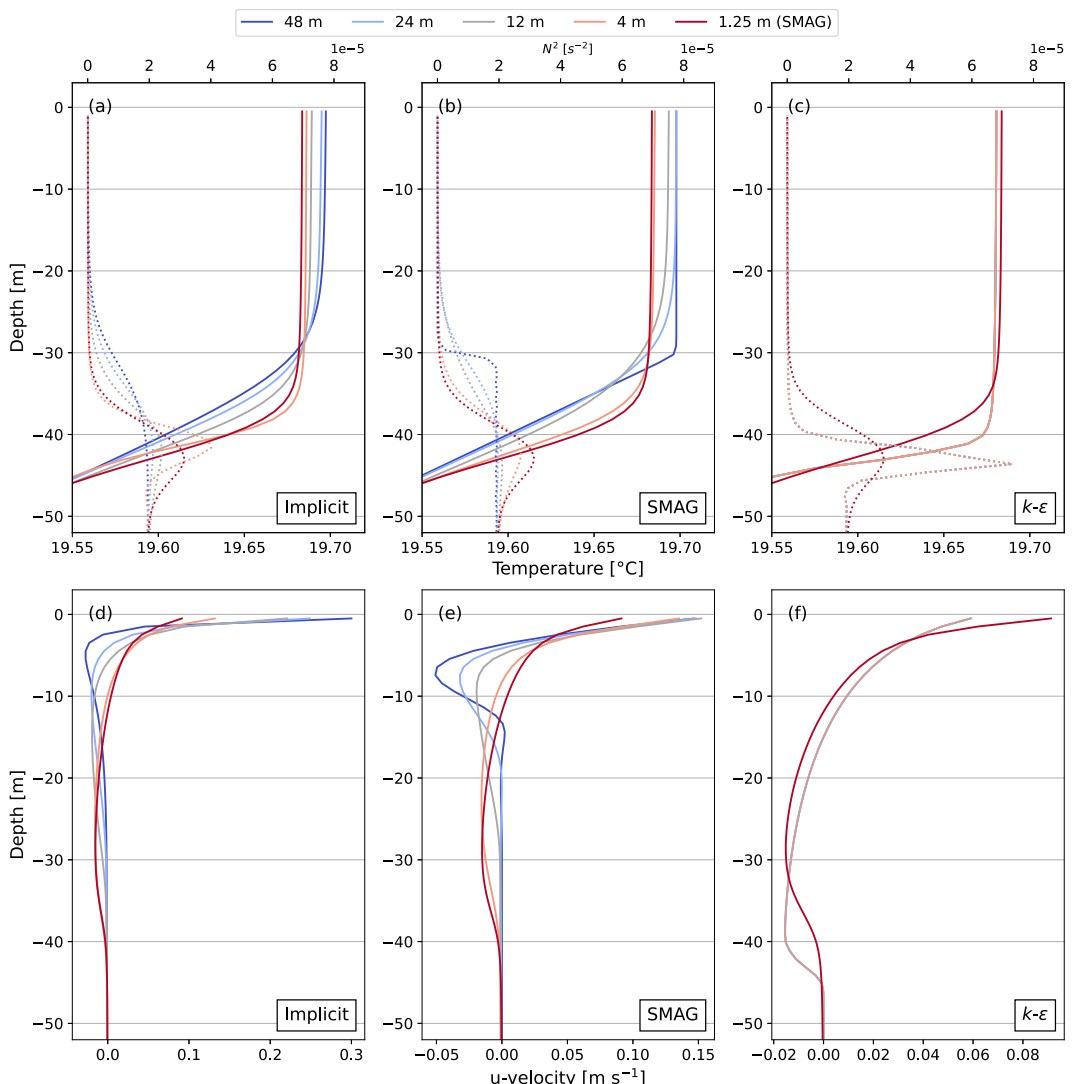


Figure 7. Averaged temperature and u-velocity profiles for the shear-only case by the implicit method (a, d), the Smagorinsky model (b, e), and the ϵ model (c, f). Along with the temperature profiles (solid lines) in the top panels, the accompanying N^2 profiles are shown as dotted lines. The 1.25 m Smagorinsky run is used as the baseline of comparison in red lines. Note the differences in the x -axis scale in the bottom row.

effectively, as further reflected in the MLD time series (Figure 12b). Similarly, the implicit method at $\Delta = 48$ m also struggles to drive mixed-layer deepening, despite some turbulence appearing in the velocity field in Figure 3 (so is the non-zero variance in Figure 8a).

Despite difficulties in representing mixed-layer deepening at coarse grid spacings, both Smagorinsky and the implicit method demonstrate better performance at finer grids. From $\Delta = 48$ to 4 m, the temperature and velocity profiles (Figures 7a, 7b, 7d, and 7e), as well as the temperature and momentum fluxes (Figures 8d, 8e, 8g, and 8h), converge to the baseline solution. The momentum fluxes increase within the mixed-layer interior (10–30 m), indicating stronger downward mixing of momentum input from surface wind stress. Near the surface (above 10 m), the Smagorinsky subgrid flux for momentum contributes less to the total momentum flux with smaller grid spacing, suggesting that vertical mixing is increasingly dominated by resolved turbulence rather than the subgrid closure, as expected for LES. However, the opposite trend is observed in temperature flux, where the subgrid contribution in the Smagorinsky runs increases with resolution near the entrainment layer at about 40 m. This can be explained by the enhanced eddy diffusivity (see Supporting Information S1) and a larger temperature

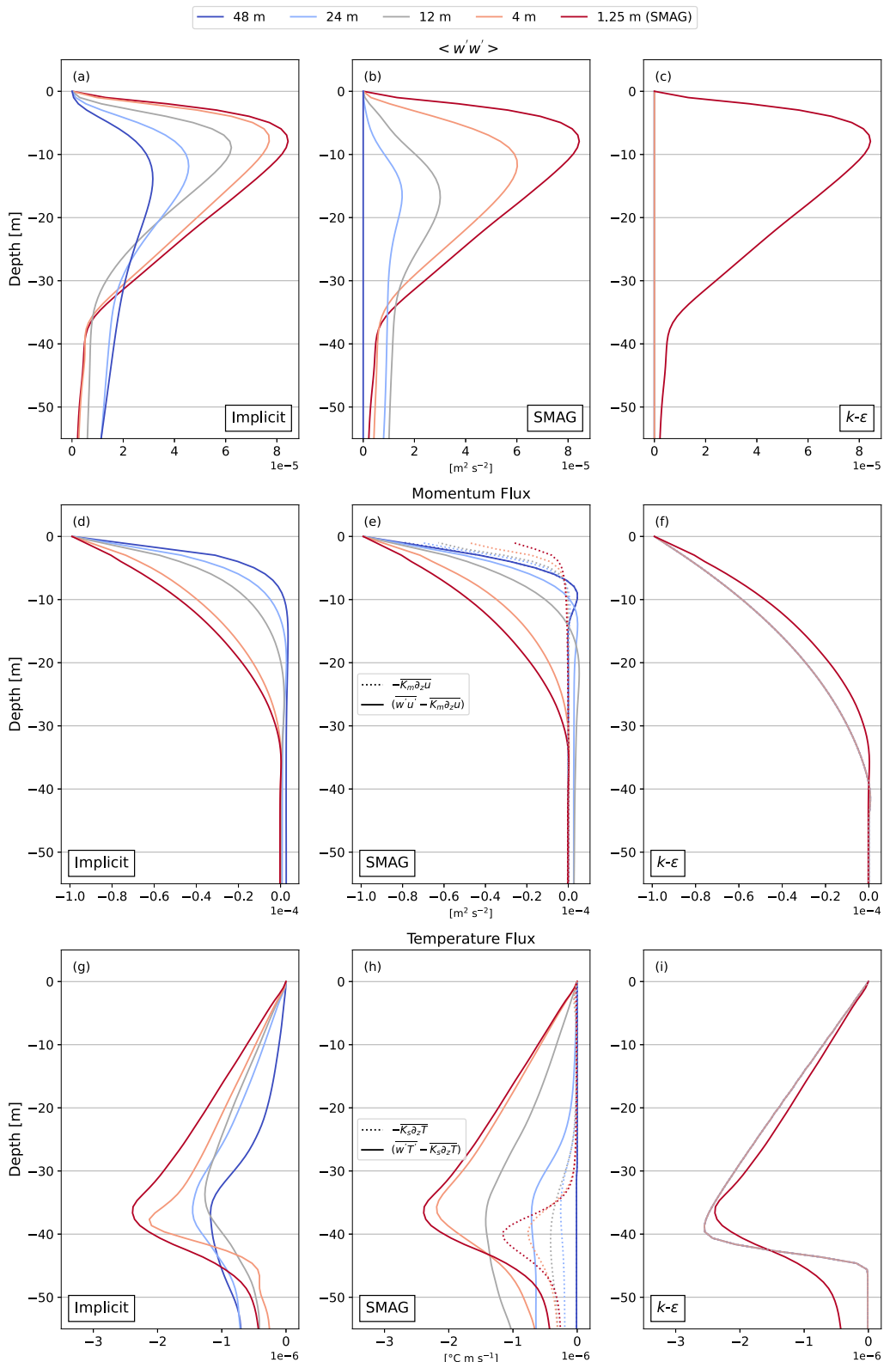


Figure 8. Averaged vertical velocity variance, together with the momentum and temperature fluxes from the shear case by the implicit method (a, d, g), the Smagorinsky model (b, e, h), and the $k-\epsilon$ model (c, f, i). In the flux profiles, the solid lines show the total flux and the dotted lines show the subgrid component. The 1.25 m Smagorinsky run is used as the baseline of comparison in red lines. Note that all $k-\epsilon$ runs produce the same profile consisting only of the subgrid component.

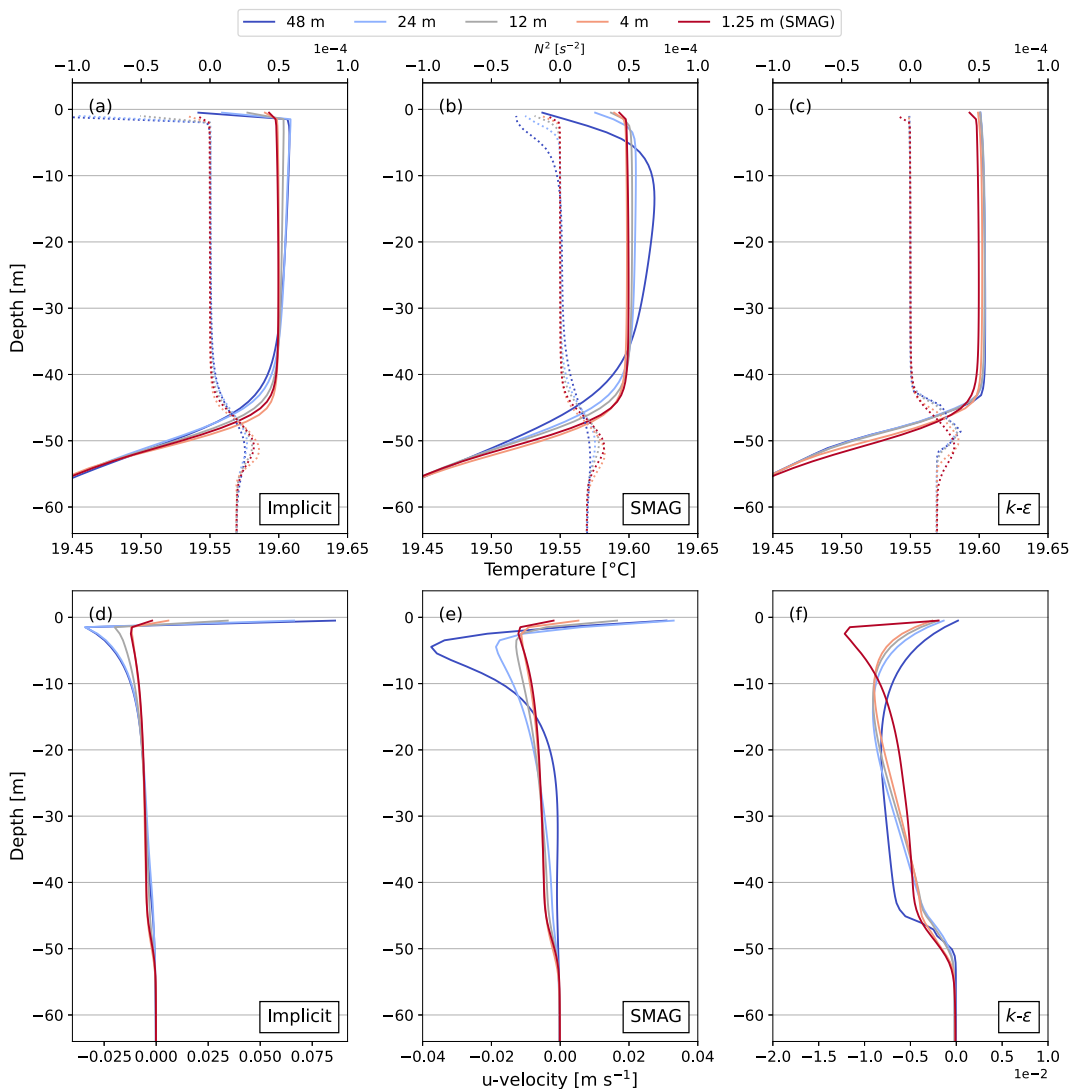


Figure 9. Averaged temperature and u-velocity profiles for the convection-wind-wave case by the implicit method (a, d), the Smagorinsky model (b, e), and the $k-\epsilon$ model (c, f). Along with the temperature profiles (solid lines) in the top panels, the accompanying N^2 profiles are shown as dotted lines. The 1.25 m Smagorinsky run is used as the baseline of comparison in red lines. Note the differences in the x-axis scale in the bottom row.

gradient (Figure 9b for the stronger stratification at the entrainment layer) at finer grid spacings in the Smagorinsky runs.

When comparing the performance of different closures, the shear-only case highlights $k-\epsilon$'s consistency for representing boundary layer mixing with little sensitivity to grid resolution. At coarse resolution, $k-\epsilon$ can offer better accuracy than Smagorinsky and the implicit method for the mean-state profiles. However, the latter LES approaches improve significantly at a higher resolution as their solutions converge to the baseline. For nesting applications, $k-\epsilon$ may suppress the emergence of turbulent eddies, making it problematic for intermediate nesting steps. Instead, transitioning from RANS or one-equation closures to Smagorinsky or the implicit method can help to resolve turbulence explicitly in the boundary layer. Nevertheless, this approach introduces a trade-off with mean-state accuracy, which must be considered despite the benefits at higher resolutions. While shear-only forcing is uncommon at the ocean surface (Belcher et al., 2012), these findings may have implications for bottom boundary layer simulations (Umlauf et al., 2015; Wenegrat & Thomas, 2020).

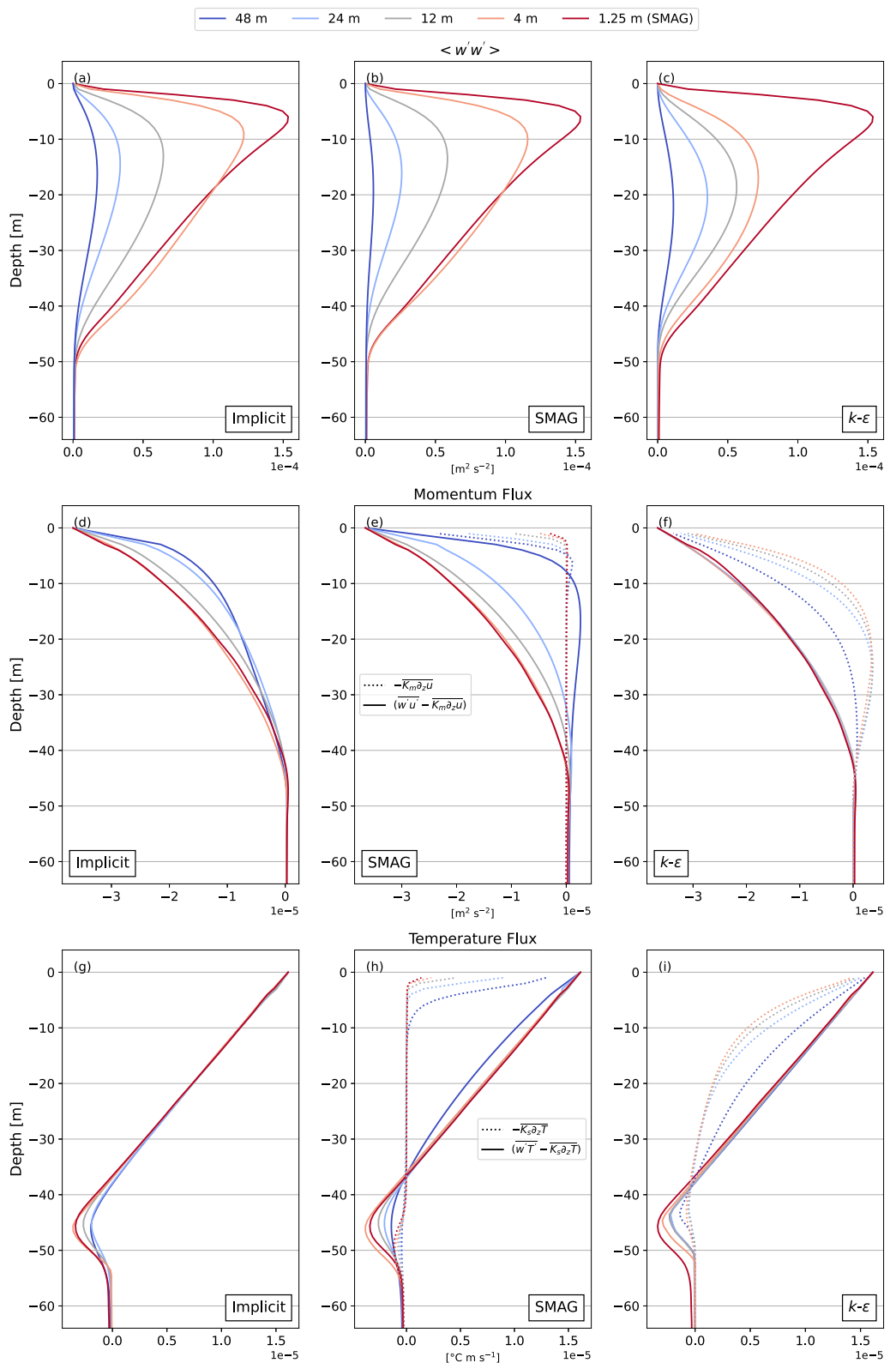


Figure 10. Averaged vertical velocity variance, together with the momentum and temperature fluxes from the convection-wind-wave case by the implicit method (a, d, g), the Smagorinsky model (b, e, h), and the $k-\epsilon$ model (c, f, i). In the flux profiles, the solid lines show the total flux and the dotted lines show the subgrid component. The 1.25 m Smagorinsky run is used as the baseline of comparison in red lines.

3.2.3. Convection-Wind-Wave

Beyond the single forcing cases, we extend our analysis to a more oceanographically relevant case driven by the combined convection-wind-wave forcing (Figure 1). Similar figures for the convection-shear and wind-wave cases are available in Supporting Information S1.

When comparing the mixed layer profiles of different closures for this case in Figure 9 (note the different x -axes for velocity), the k - ϵ solutions demonstrate a better alignment with the baseline solution at the coarse resolution, even with partially resolved turbulence in the gray zone (see the instantaneous flow field in Figure S4 from Supporting Information S1). Further, k - ϵ exhibits minimal sensitivity to grid spacing and maintains good accuracy throughout the gray zone. In comparison, the Smagorinsky and implicit solutions show a strong sensitivity to grid spacing. For example, at $\Delta = 48$ m, instead of producing a well-mixed boundary layer, both the Smagorinsky and the implicit solutions exhibit strong temperature inversions and velocity shear near the surface (Figures 9a, 9b, 9d, and 9e), indicating poor performance when turbulent eddies are barely resolved. When Δ is refined to 4 m, both Smagorinsky and the implicit method generate a well-mixed boundary layer, with nearly identical profiles converging to the baseline solution.

The variance and flux profiles in Figure 10 highlight the role of subgrid closure in driving mixing relative to resolved motions. Similar to the convection-only case, the vertical velocity variance, which corresponds to the intensity of turbulent eddies, increases with resolution for all three closures (Figures 10–10c). k - ϵ again stands out for its consistency in representing total fluxes across the gray zone range. k - ϵ also maintains a reasonable partition between resolved and subgrid fluxes, with a smaller relative contribution from the subgrid closure at higher resolution, suggesting its adaptability to grid refinement (Figures 10f and 10i). For Smagorinsky and the implicit method, despite poor performance at coarse resolutions, the total flux converges with smaller grid spacings (Figures 10d, 10e, 10g, and 10h). Notably, the subgrid fluxes by Smagorinsky are considerably smaller than those by k - ϵ at the same grid. At the fine resolution of $\Delta = 4$ m, the Smagorinsky solutions and the implicit solutions achieve a similar accuracy relative to the baseline. Here, the small subgrid flux contribution by Smagorinsky may suggest that vertical mixing can be well represented by resolved eddies rather than the subgrid closure. However, it should also be noted that the WENO5 scheme used here may be providing a significant implicit diffusion component. Testing with higher-order schemes is recommended.

Overall, among different closures for the realistic forcings, k - ϵ can best represent the mixed-layer profiles but damps turbulent eddies. This may be advantageous for submesoscale-resolving simulations that require an accurate mixed-layer representation without explicitly resolving turbulent eddies. Despite poor performance at coarse grids, the Smagorinsky and the implicit solutions quickly converge, with a greater fraction of total flux carried by resolved turbulence. These properties may be useful for nesting applications transitioning through gray zone resolutions toward well-resolved LES, where parent solutions can influence turbulence in the nested domain (F. Chow et al., 2019).

3.3. Time Dependence

While the previous analysis focuses on instantaneous and temporally-averaged properties, in this section we compare the MLD time series to highlight the joint impacts of grid spacing and closure on the rate of mixed-layer deepening. There are many different methods to diagnose MLD, and the criteria based on a density difference from the surface is commonly used in regional models (Courtois et al., 2017). In this study, the surface density value is not used, given that some gray zone simulations are not well mixed near the surface (see Figure 9 for the temperature inversion in the 48 m Smagorinsky run from the convection-wind-wave case). Instead, we define MLD as the depth where the density exceeds the mixed layer average (taken between 15 and 25 m) by 0.005 kg m^{-3} . A range of density thresholds (0.01 – 0.001 kg m^{-3}) was tested, and the results were found to be qualitatively robust to any reasonable choice of thresholds. We have tested another common MLD criterion based on a density gradient (i.e., depth of N^2 maximum) following Fan et al. (2023). However, we find the coarse resolution runs tend to generate less pronounced N^2 maxima near the mixed layer bottom (see the stratification profiles in Figures 7a and 7b), leading to large fluctuations in the MLD time series at the initial time steps. Therefore, to allow a better comparison of MLD evolution across different gray zone simulations, we choose the criteria of density threshold.

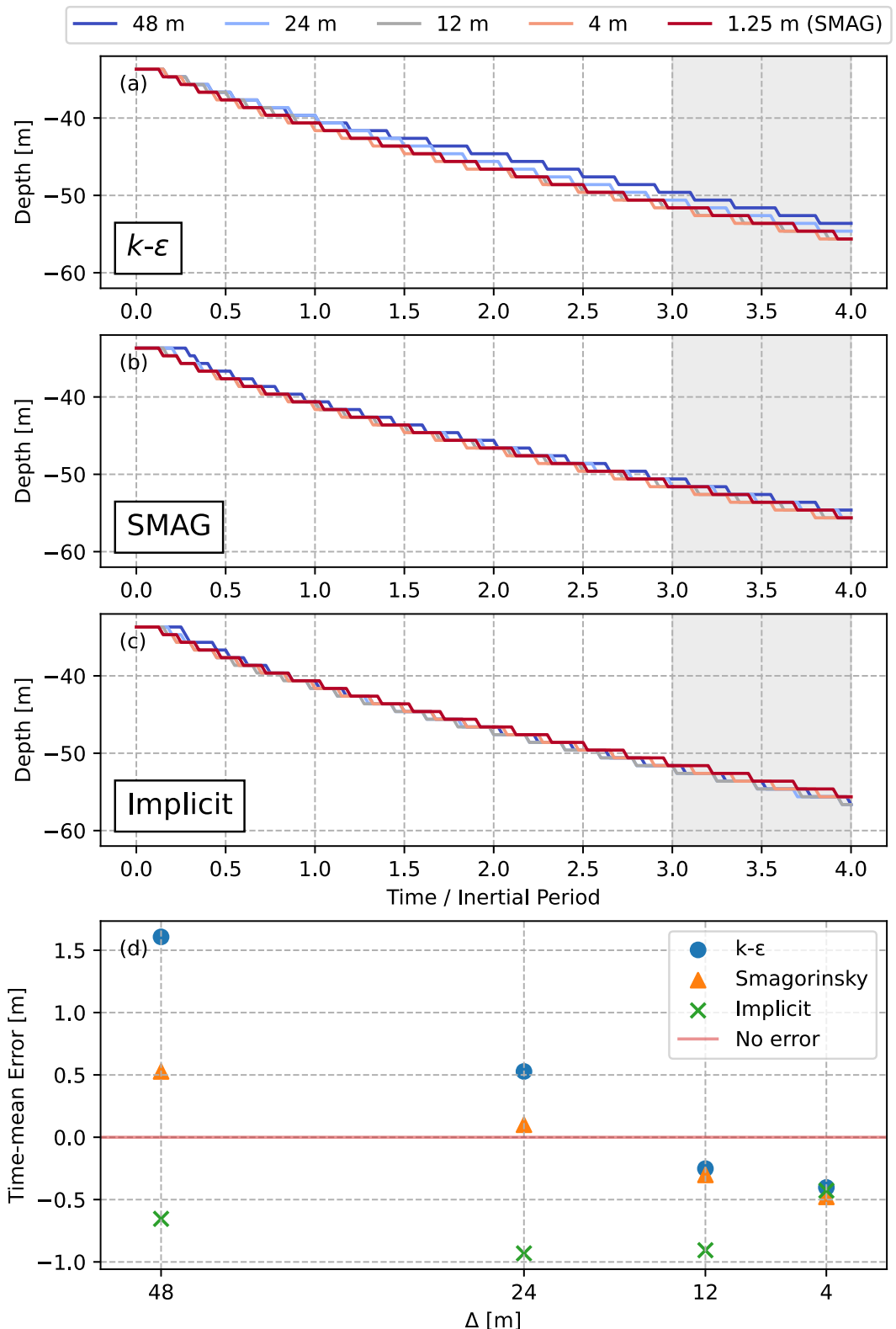


Figure 11. Time series of MLD in the convection-only case by different closures and grid resolutions in panel (a–c). The mean MLD errors relative to the baseline run in the last inertial period are shown in panel (d).

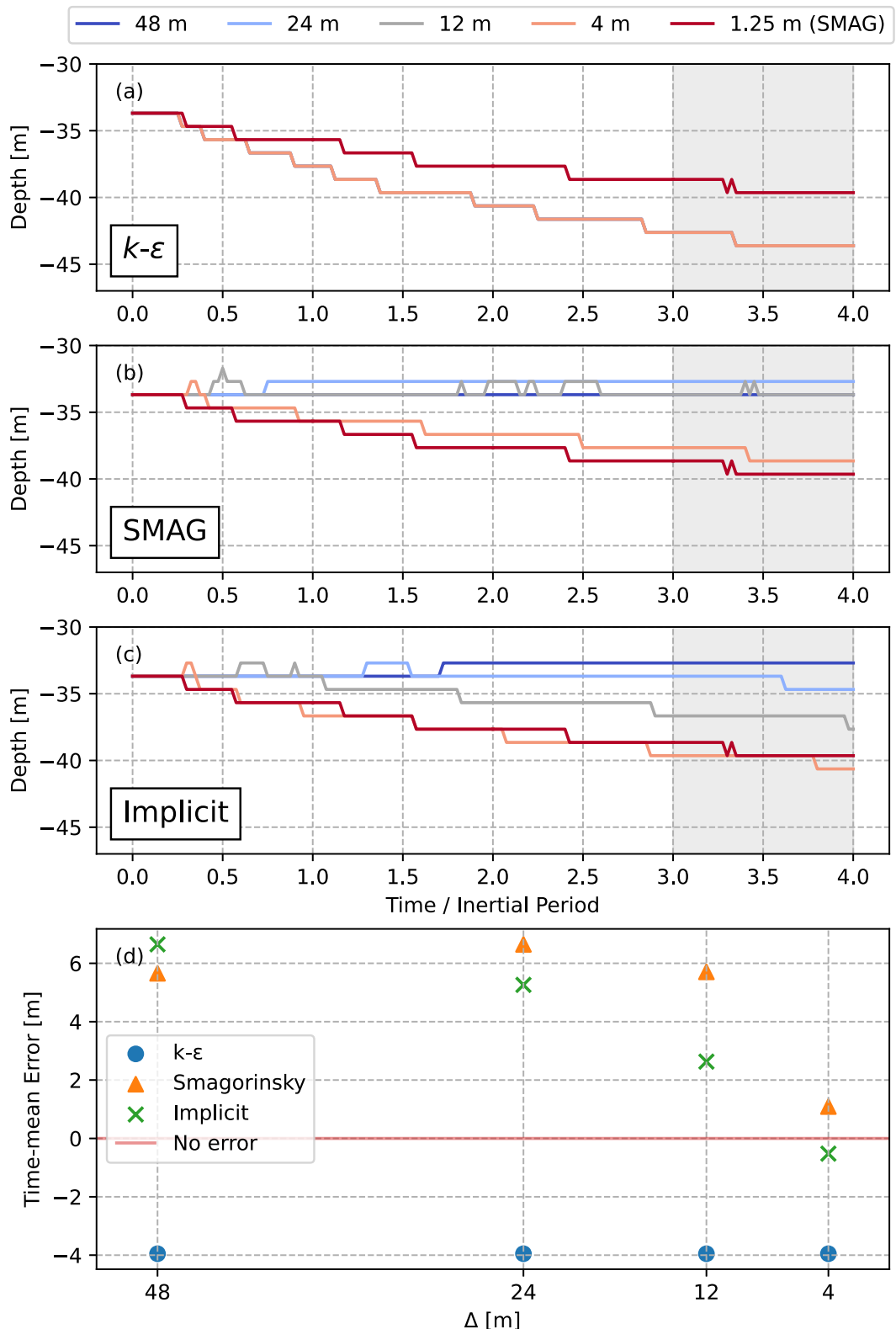


Figure 12. Time series of MLD in the shear-only case by different closures and grid resolutions in panels (a–c). The mean MLD errors relative to the baseline run in the last inertial period are shown in panel (d).

Figure 11 shows the MLD time series for the convection-only case comparing different closures (panels a–c) and summarizing the mean errors over the last inertial period (panel d). Similarly to the mixed-layer profiles discussed in Section 3.2.1, the mixed-layer deepening rate shows minimal sensitivity to grid spacing for all closures. Shortly after model initialization, MLD starts to deepen in all gray zone simulations due to surface buoyancy loss, reaching approximately 55 m after four inertial periods. While all closure solutions converge at smaller grid spacing, the $k\text{-}\epsilon$ solution at $\Delta = 48$ m exhibits the largest error from the baseline, though still relatively small (1–2 m). This error is consistent with earlier observations in the temperature profiles (Figure 6c), where $k\text{-}\epsilon$ struggles in the entrainment layer between 45 and 55 m.

In contrast to convection, the mixed-layer evolution under wind forcing alone (Figure 12) is more sensitive to closure and grid spacing. As discussed earlier, the $k\text{-}\epsilon$ runs in the shear-only case do not produce turbulent eddies, modeling turbulence mixing entirely as a subgrid process. This results in an identical solution regardless of grid spacing. In Figure 12, the $k\text{-}\epsilon$ solutions exhibit a deeper mixed layer after four inertial periods, consistent with the stratification seen in the temperature profiles (Figure 7c). For Smagorinsky and the implicit solutions, their inefficiency in driving vertical mixing at coarse grid spacings (e.g., $\Delta = 48, 24$, and 12 m) is evident for the lack of mixed-layer deepening in the MLD time series (Figures 12b and 12c), although we note these simulations also had a thick transition layer between the mixed-layer and interior with reduced stratification (Figures 7a and 7b). Overall, MLD evolution in the shear-only case highlights the accumulation of mean-state error in gray zone simulations, which could become particularly problematic for long-time integrations or applications where the fidelity of large-scale conditions is critical for LES.

Figure 13 shows mixed-layer evolution under the more realistic convection-wind-wave forcing condition. In addition to mean-state drift, the MLD time series reveals notable differences in the onset of mixed-layer deepening. For $k\text{-}\epsilon$, the mixed layer begins to deepen immediately, following the baseline solution. However, for Smagorinsky and the implicit method, the deepening of MLD is delayed at coarse resolutions. For example, in the Smagorinsky solution at $\Delta = 48$ m, MLD remains at its initial value for 1.5 inertial periods, leading to a shallower MLD for about 5 m ($\sim 10\%$ MLD) after four inertial periods. This suggests that the transition to turbulence also depends on grid spacing and closure (see Figure S16 in Supporting Information S1 for the time series of vertical velocity variance), which can be an important consideration for strongly time-dependent turbulence problems such as the diurnal cycle (Sutherland et al., 2016; Wenegrat & McPhaden, 2015). At coarse grid spacings that barely resolve turbulent eddies, $k\text{-}\epsilon$ may offer a better mean-state representation of the mixed layer. When using Smagorinsky or the implicit method in the intermediate nesting steps toward LES, introducing additional perturbations to initial and boundary conditions may help spin up turbulent eddies and improve inner-domain solutions. Further, while not being tested, the strength of the interior stratification can affect the turbulent length scale in the entrainment zone and hence may introduce an additional dimension to the resolution and closure sensitivity noted here.

3.4. Effective Resolution

A model's effective resolution is commonly defined as the horizontal length scale where dissipation—due to both the numerical discretization and turbulence parameterizations—begin to significantly influence the solution, such that the underlying dynamics are no longer properly represented. It is often diagnosed by where the kinetic energy spectrum departs from the expected slope at small scales, for example, $k^{-5/3}$ for atmospheric mesoscale dynamics (Skamarock, 2004) and k^{-2} for oceanic submesoscale (Soufflet et al., 2016). Prior work indicates the effective model resolution is often reasonably approximated as multiples of grid spacing ($\approx 7 - 10\Delta$), although the precise value can be a complicated factor of many choices of numerical setup, including advection schemes for momentum and tracers, as well as time-stepping routine (Soufflet et al., 2016). Here, we highlight how gray zone simulations can incorrectly represent the dynamics near the turbulence injection scale (e.g., Section 3.1), such that even scales much larger than those expected to be affected directly by model dissipation may be contaminated. In this section, we highlight this behavior focusing on the convection-wind-wave case. The results of other forcing cases display similar characteristics and can be found in Figures S17–S20 in Supporting Information S1.

The effective resolution of the baseline run—due to explicit dissipation from the eddy viscosity and the implicit numerical dissipation from the WENO5 scheme—can be identified by the high-wavenumber roll-off of the spectral kinetic energy (Figure 14). The baseline KE spectra, labeled as 1.25 m (SMAG) in all panels, follow the expected slope of the inertial subrange ($k^{-5/3}$) starting from 50 m until wavelengths of approximately 10 m at

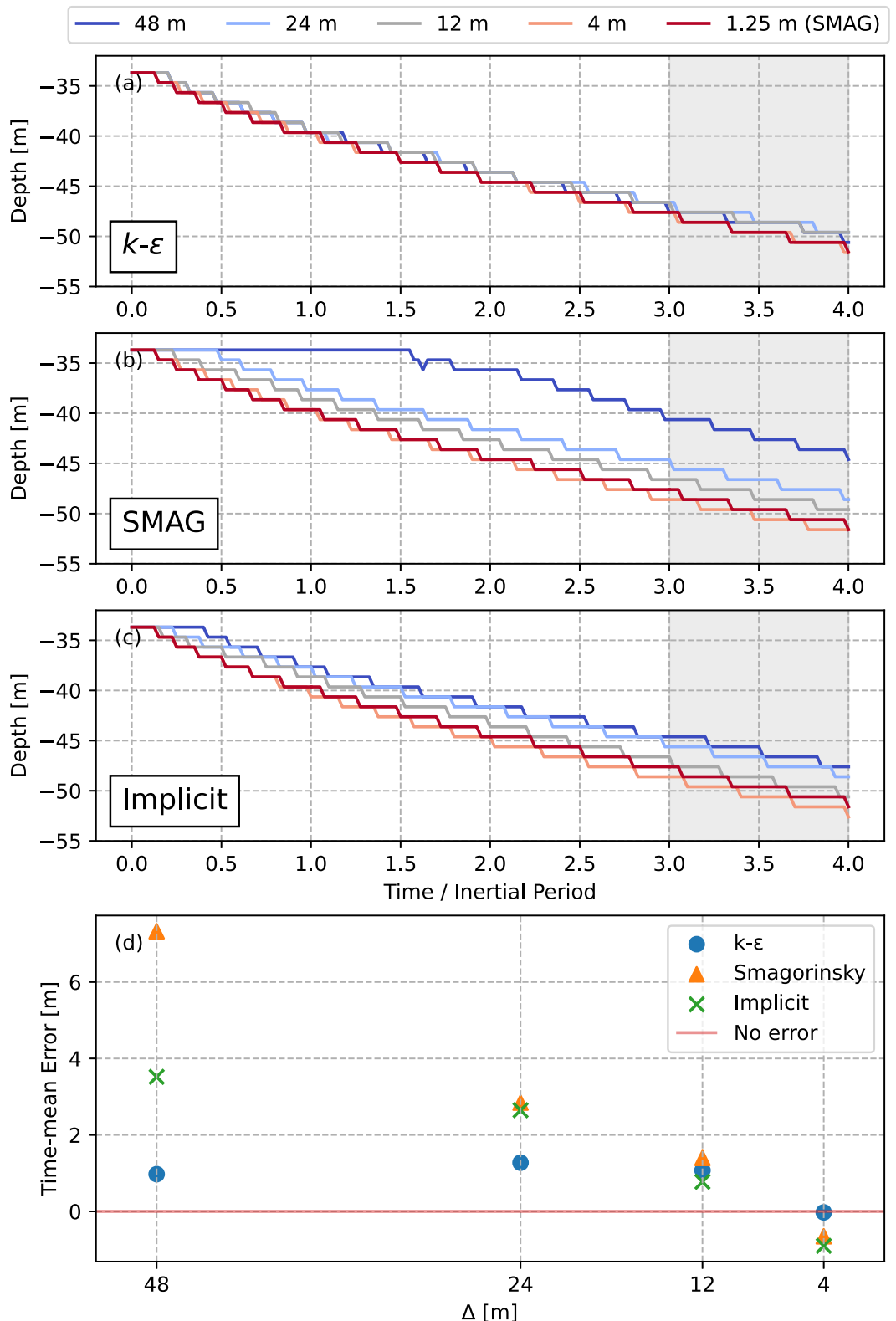


Figure 13. Time series of MLD in the convection-wind-wave case by different closures and grid resolutions (panels a–c). The mean errors relative to the baseline run is calculated for the last inertial period (panel d).

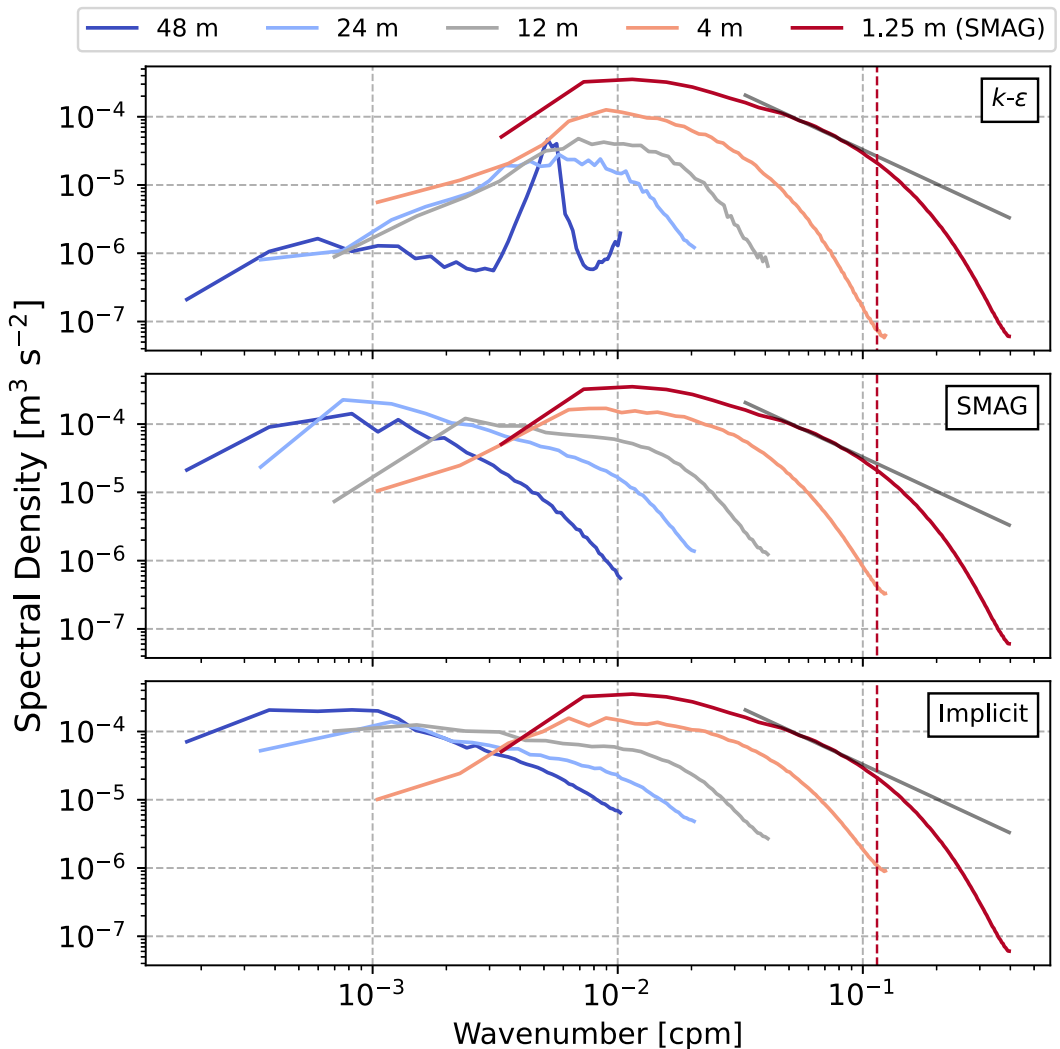


Figure 14. Turbulent kinetic energy spectra from the convection-wind-wave case at 20 m depth, derived from the 3D velocity fields and averaged over the last inertial period. The dashed vertical lines mark the effective numerical resolution of the 1.25 m Smagorinsky run at 7Δ , and the characteristic $-5/3$ slope of the inertial subrange is shown in gray.

which point there is a faster roll-off. The separation between the inertial subrange and the numerical range indicates an effective numerical resolution of about 7Δ , similar to the range found previously for much larger-scale simulations (Soufflet et al., 2016). However, only the baseline run has an unambiguous effective resolution scale that can be identified from the spectral slopes. For the gray-zone runs of larger grid spacings (e.g., the implicit runs $\Delta > 4$ m), the inertial subrange is not well resolved while still impacted by the numerical dissipation, making it impossible to identify the effective resolution based on the expected spectral slope. This highlights the presence of under-resolved large eddies and indicates the gray zone nature of these simulations. The misrepresentation of large eddies and model dissipation is likely to contribute to errors in the mean-state profiles (see Section 3.2.3).

In Figure 14, the $k-\epsilon$ spectra display lower levels of energy than the baseline and the implicit and Smagorinsky spectra at the same grid spacings, suggesting that the use of $k-\epsilon$ in the gray zone substantially damps turbulent eddies. This is consistent with the smoothed velocity gradients found in the flow structure (Section 3.1). At $\Delta = 48$ m, the $k-\epsilon$ spectrum becomes overly flat with few turbulent eddies explicitly resolved. The damping issue of $k-\epsilon$ is the most pronounced in the shear-only case where the closure completely suppresses the emergence of turbulent eddies regardless of grid spacings (Figure 3). For the $k-\epsilon$ simulations, the effective resolution cannot be meaningfully defined here, as the dynamics of all scales up to the domain size are not properly represented. For nested simulations across the gray zone, the use of $k-\epsilon$ may be problematic for supplying overly laminar flows for

boundary conditions, affecting the turbulence statistics in inner solutions. The importance of this will vary depending on the role of turbulence advection between parent and child domains.

Compared to $k-\epsilon$, the Smagorinsky closure and the implicit method generate similar spectra of higher energy levels for the resolved turbulent motions (Figure 14). This is valuable during intermediate nesting steps in the gray zone to better represent turbulence in the inner domain despite the trade-off in the mean-state accuracy (Section 3.2.3). However, instead of aligning with the baseline solution, the spectral peaks in the Smagorinsky and the implicit runs shift toward longer wavelengths at larger grid spacings as the model still attempts to resolve some large turbulence eddies, albeit less realistically, at the coarse resolution of the gray zone. The spectrum shift highlights how the spectral definition of effective resolution (based on roll-off of the slope) may at times be misleading, as there can be shifts in wavenumber space or energy levels that are independent of the spectral shape (see also Figure S17 in Supporting Information S1). For instance, the 24 m grid solution using Smagorinsky has a spectral shape broadly similar to the 1.25 m baseline run, but being shifted such that the spectral peak is at approximately 1,200 m wavelength rather than 150 m. It would be incorrect to conclude that the effective resolution of this simulation is near 200 m (where there is a roll-off in the spectrum), as comparison with the baseline simulation indicates inaccurate representation of turbulent motions at scales well exceeding 10Δ (in the sense of both the variance contained at a given spatial scale and in terms of the coherent structures as discussed in Section 3.1). This should be considered for nesting applications, where inaccurate representations of boundary layer turbulence from the outer domain can be advected into the inner domain through the boundary conditions, contaminating the final solution, an issue identified previously for nested LES of the atmospheric boundary layer (Mazzaro et al., 2017; Mirocha et al., 2013).

4. Summary and Discussion

This study evaluates the gray zone performance of two common turbulence closures, $k-\epsilon$ and Smagorinsky, as well as the implicit method using the WENO5 advection scheme, for ocean surface mixed layer under different forcing conditions. With marginally resolved turbulent eddies, we find that coherent turbulent structures, mean mixed-layer profiles, and kinetic energy spectra exhibit closure-dependent resolution sensitivities. In general, the $k-\epsilon$ solutions provide the highest accuracy in representing bulk properties such as mixed layer depth, maintaining well-mixed temperature and velocity profiles across the gray zone range. The total fluxes (subgrid plus resolved) by $k-\epsilon$ also remain mostly consistent, with reasonable adjustment to resolution in the partitioning between the subgrid and resolved fluxes. However, the instantaneous flow fields and the kinetic energy spectra suggest $k-\epsilon$ damps the turbulence motions, representing mixing primarily as a subgrid process, even when the grid is fine enough to begin resolving turbulence. The most striking example is the shear-only case, where $k-\epsilon$ suppresses turbulence entirely, producing an identical laminar flow field at all grid spacings tested. In comparison, the Smagorinsky and the implicit solutions show greater sensitivity to grid spacing. With coarse grids, they fail to drive sufficient vertical mixing to deepen the mixed layer, resulting in strong velocity shear and temperature inversions near the surface. However, with smaller grid spacing, both Smagorinsky and the implicit method demonstrate improvement as their solutions converge toward the baseline LES. Unlike the $k-\epsilon$ solutions, which are dominated by subgrid fluxes, the Smagorinsky and the implicit solutions primarily represent turbulent mixing through the resolved flow motions, exhibiting enhanced kinetic energy at the smaller scales.

The gray zone simulations are designed to inform modeling strategies on turbulence closures during the intermediate scale between the typical RANS and LES paradigms. Depending on modeling objectives, the consistency of $k-\epsilon$ is valuable for simulations aiming to resolve processes larger than boundary layer turbulence (e.g., Langmuir cells and submesoscale fronts). Even at the gray-zone resolutions with partially resolved turbulent eddies, $k-\epsilon$ shows good performance in representing bulk mixing in the boundary layer. However, the $k-\epsilon$ solutions are associated with damped turbulence in the resolved velocity fields. While the absence of resolved turbulence may be acceptable for some submesoscale-resolving simulations, it can be problematic for nested simulations that need to traverse the gray zone to achieve realistic LES. For example, in a nested setup, an overly laminar parent-domain flow can inhibit small-scale turbulence development in the child domain (Zhou et al., 2014). In this case, using $k-\epsilon$ in the gray zone may effectively act as a much lower-resolution simulation than the grid spacing suggests. A potential remedy is to switch from $k-\epsilon$ to Smagorinsky or use no closure (implicit method) during intermediate nesting steps, allowing for more active turbulence at the boundaries. However, this comes with the trade-off of less accurately resolved mean-state evolution, potentially leading to drift in larger-scale properties. Given the fast convergence at smaller grid spacing, this trade-off may be acceptable,

especially considering that high-resolution nests are typically run for short durations, limiting mean-state error accumulation. Strongly time-dependent problems introduce an additional challenge: turbulence onset exhibits sensitivity to both grid spacing and closure, making it difficult to predict a priori. This should be carefully considered when designing nesting strategies.

Here we have focused on the performance of common RANS and LES closures; however, several open questions remain regarding best practices for modeling in the ocean gray zone. First, further case studies should investigate submesoscale frontal configurations and the associated instabilities (e.g., symmetric instability), as their length scales likely fall within the gray zone and significantly impact turbulence properties in ways not well captured by RANS closures (Bachman et al., 2017; Chor et al., 2022; Dong et al., 2022). Second, despite our effort to design surface forcing representative of the realistic ocean, similar sensitivity analyses at the gray zone resolution should be applied to realistic regional simulations formally validated by observational data. Additional forcing scenarios such as stabilizing buoyancy forcing and time-dependent turbulence problems (i.e., the diurnal cycle) should also be considered in future studies. Third, the prescription of open boundary conditions—including issues such as the forcing frequency and nudging strength—likely influences the fidelity of gray zone simulations. While this issue has been recognized in atmospheric simulations (F. Chow et al., 2019), its impact in ocean simulations remains largely unexplored (Scotti, 2010). Finally, while we have tested existing RANS and LES closures in the gray zone outside their intended applications, the existence of the gray zone problem ultimately necessitates the development of scale-aware turbulence parameterizations and hybrid RANS/LES methods, such as detached-eddy simulation (Spalart, 2009). High-resolution ocean simulation will benefit from a uniform turbulence model that can be seamlessly applied across the gray zone without trade-offs between mean-state and turbulence representation, while also minimizing the need for extensive sensitivity testing and ad hoc tuning. Efforts in this direction can be guided by existing research on scale-aware turbulence closures for atmospheric modeling (F. Chow et al., 2019; Honnert et al., 2020).

Data Availability Statement

The original source code for Coastal and Regional Ocean CCommunity model (CROCO) v1.3.0 used to generate the gray zone simulations is preserved at Zenodo by Auclair et al. (2022). The input files, configuration options, and data analysis scripts to reproduce the gray zone results are publicly available at Zenodo by Chen et al. (2025).

Acknowledgments

Z.C. was supported by the National Science Foundation (NSF) Grant OCE-2232441. J.O.W. was partially supported by the NSF Grants OCE-2232441 and OCE-2148945. T.C. was supported by NSF OCE-2242182. We would like to acknowledge high-performance computing support from the Derecho system (<https://doi.org/10.5065/qp9-apg09>) and the Casper system (<https://ncar.pub/casper>), both of which are provided by the National Center for Atmospheric Research sponsored by the NSF. We are grateful for three anonymous reviewers who provided valuable comments to improve the quality of this manuscript.

References

- Auclair, F., Benshila, R., Bordois, L., Boutet, M., Brémont, M., Caillaud, M., et al. (2022). Coastal and Regional Ocean CCommunity model. *Zenodo*. <https://doi.org/10.5281/zenodo.7415343>
- Bachman, S. D., Fox-Kemper, B., Taylor, J. R., & Thomas, L. N. (2017). Parameterization of frontal symmetric instabilities. I: Theory for resolved fronts. *Ocean Modelling*, 109, 72–95. <https://doi.org/10.1016/j.ocemod.2016.12.003>
- Beare, R. J. (2014). A length scale defining partially-resolved boundary-layer turbulence simulations. *Boundary-Layer Meteorology*, 151(1), 39–55. <https://doi.org/10.1007/s10546-013-9881-3>
- Belcher, S. E., Grant, A. L. M., Hanley, K. E., Fox-Kemper, B., Van Roekel, L., Sullivan, P. P., et al. (2012). A global perspective on Langmuir turbulence in the ocean surface boundary layer. *Geophysical Research Letters*, 39(18), L18605. <https://doi.org/10.1029/2012GL052932>
- Bhattacharya, R., & Stevens, B. (2016). A two turbulence kinetic energy model as a scale-adaptive approach to modeling the planetary boundary layer. *Journal of Advances in Modeling Earth Systems*, 8(1), 224–243. <https://doi.org/10.1002/2015MS000548>
- Brisson, E., Demuzere, M., & van Lipzig, N. P. M. (2016). Modelling strategies for performing convection-permitting climate simulations. *Meteorologische Zeitschrift*, 25(2), 149–163. <https://doi.org/10.1127/metz/2015/0598>
- Canuto, V. M., Howard, A., Cheng, Y., & Dubovikov, M. S. (2001). Ocean turbulence. Part I: One-point closure model—Momentum and heat vertical diffusivities. *Journal of Physical Oceanography*, 31(6), 1413–1426. [https://doi.org/10.1175/1520-0485\(2001\)031\(1413:OTPIOP\)2.0.CO;2](https://doi.org/10.1175/1520-0485(2001)031(1413:OTPIOP)2.0.CO;2)
- Chamecki, M., Chor, T., Yang, D., & Meneveau, C. (2019). Material transport in the ocean mixed layer: Recent developments enabled by large eddy simulations. *Reviews of Geophysics*, 57(4), 1338–1371. <https://doi.org/10.1029/2019RG000655>
- Chen, Z., Wenegrat, J., Chor, T., & Marchesiello, P. (2025). Evaluating turbulence parameterizations at gray zone resolutions for the ocean surface boundary layer: Model configuration and data analysis (technical report). *Zenodo*. <https://doi.org/10.5281/zenodo.15116237>
- Chor, T., McWilliams, J. C., & Chamecki, M. (2021). Modifications to the K-profile parameterization with nondiffusive fluxes for Langmuir turbulence. *Journal of Physical Oceanography*, 51(5), 1503–1521. <https://doi.org/10.1175/JPO-D-20-0250.1>
- Chor, T., Wenegrat, J. O., & Taylor, J. (2022). Insights into the mixing efficiency of submesoscale centrifugal-symmetric instabilities. *Journal of Physical Oceanography*, 52(10), 2273–2287. <https://doi.org/10.1175/JPO-D-21-0259.1>
- Chor, T., Yang, D., Meneveau, C., & Chamecki, M. (2018). Preferential concentration of noninertial buoyant particles in the ocean mixed layer under free convection. *Physical Review Fluids*, 3(6), 064501. <https://doi.org/10.1103/PhysRevFluids.3.064501>
- Chow, F., Schär, C., Ban, N., Lundquist, K., Schlemmer, L., & Shi, X. (2019). Crossing multiple gray zones in the transition from mesoscale to microscale simulation over complex terrain. *Atmosphere*, 10(5), 274. <https://doi.org/10.3390/atmos10050274>
- Chow, F. K., Street, R. L., Xue, M., & Ferziger, J. H. (2005). Explicit filtering and reconstruction turbulence modeling for large-eddy simulation of neutral boundary layer flow. *Journal of the Atmospheric Sciences*, 62(7), 2058–2077. <https://doi.org/10.1175/JAS3456.1>

- Courtois, P., Hu, X., Pennelly, C., Spence, P., & Myers, P. G. (2017). Mixed layer depth calculation in deep convection regions in ocean numerical models. *Ocean Modelling*, 120, 60–78. <https://doi.org/10.1016/j.ocemod.2017.10.007>
- Daniels, M. H., Lundquist, K. A., Mirocha, J. D., Wiersema, D. J., & Chow, F. K. (2016). A new vertical grid nesting capability in the weather research and forecasting (WRF) model. *Monthly Weather Review*, 144(10), 3725–3747. <https://doi.org/10.1175/MWR-D-16-0049.1>
- Dauhajre, D. P., McWilliams, J. C., & Renault, L. (2019). Nearshore Lagrangian connectivity: Submesoscale influence and resolution sensitivity. *Journal of Geophysical Research: Oceans*, 124(7), 5180–5204. <https://doi.org/10.1029/2019JC014943>
- Dong, J., Fox-Kemper, B., Wenegrat, J. O., Bodner, A. S., Yu, X., Belcher, S., & Dong, C. (2024). Submesoscales are a significant turbulence source in global ocean surface boundary layer. *Nature Communications*, 15(1), 9566. <https://doi.org/10.1038/s41467-024-53959-y>
- Dong, J., Jing, Z., Fox-Kemper, B., Wang, Y., Cao, H., & Dong, C. (2022). Effects of symmetric instability in the Kuroshio extension region in winter. *Deep Sea Research Part II: Topical Studies in Oceanography*, 202, 105142. <https://doi.org/10.1016/j.dsrt.2022.105142>
- Fan, X., Fox-Kemper, B., Suzuki, N., Li, Q., Marchesiello, P., Auclair, F., et al. (2023). Comparison of the coastal and regional ocean community model (CROCO) and NCAR-LES in non-hydrostatic simulations. In *EGUspHERE* (pp. 1–38). <https://doi.org/10.5194/egusphere-2023-1657>
- Goodfriend, E., Chow, F. K., Vanella, M., & Balaras, E. (2015). Improving large-eddy simulation of neutral boundary layer flow across grid interfaces. *Monthly Weather Review*, 143(8), 3310–3326. <https://doi.org/10.1175/MWR-D-14-00392.1>
- Grinstein, F. F., Margolin, L. G., & Rider, W. J. (Eds.) (2007). *Implicit large eddy simulation: Computing turbulent fluid dynamics*. Cambridge University Press. <https://doi.org/10.1017/CBO9780511618604>
- Gula, J., Theetten, S., Cambon, G., & Roullet, G. (2021). Description of the GIGATL simulations. *Zenodo*. <https://doi.org/10.5281/zenodo.4948523>
- Herman, A., Dojczman, M., & Świdzicz, K. (2020). High-resolution simulations of interactions between surface ocean dynamics and frazil ice. *The Cryosphere*, 14(11), 3707–3729. <https://doi.org/10.5194/tc-14-3707-2020>
- Honnert, R., Efstratiou, G. A., Beare, R. J., Ito, J., Lock, A., Neggers, R., et al. (2020). The atmospheric boundary layer and the “Gray Zone” of turbulence: A critical review. *Journal of Geophysical Research: Atmospheres*, 125(13), e2019JD030317. <https://doi.org/10.1029/2019JD030317>
- Honnert, R., Masson, V., & Couvreux, F. (2011). A diagnostic for evaluating the representation of turbulence in atmospheric models at the kilometric scale. *Journal of the Atmospheric Sciences*, 68(12), 3112–3131. <https://doi.org/10.1175/JAS-D-11-061.1>
- Hypolite, D., Romero, L., McWilliams, J. C., & Dauhajre, D. P. (2021). Surface gravity wave effects on submesoscale currents in the open ocean. *Journal of Physical Oceanography*, 51(11), 3365–3383. <https://doi.org/10.1175/JPO-D-20-0306.1>
- Hypolite, D., Romero, L., McWilliams, J. C., & Dauhajre, D. P. (2022). Langmuir circulations transfer kinetic energy from submesoscales and larger scales to dissipative scales. *Journal of Physical Oceanography*, 53(1), 253–268. <https://doi.org/10.1175/JPO-D-22-0126.1>
- Ilicak, M., Özgökmen, T. M., Peters, H., Baumert, H. Z., & Iskandarani, M. (2008). Very large eddy simulation of the Red Sea overflow. *Ocean Modelling*, 20(2), 183–206. <https://doi.org/10.1016/j.ocemod.2007.08.002>
- Jones, W. P., & Launder, B. E. (1972). The prediction of laminarization with a two-equation model of turbulence. *International Journal of Heat and Mass Transfer*, 15(2), 301–314. [https://doi.org/10.1016/0017-9310\(72\)90076-2](https://doi.org/10.1016/0017-9310(72)90076-2)
- Jullien, S., Caillaud, M., Benshila, R., Bordois, L., Cambon, G., Dumas, F., et al. (2022). CROCO technical and numerical documentation. *Zenodo*. <https://doi.org/10.5281/zenodo.7400922>
- Kurowski, M. J., & Teixeira, J. (2018). A scale-adaptive turbulent kinetic energy closure for the dry convective boundary layer. *Journal of the Atmospheric Sciences*, 75(2), 675–690. <https://doi.org/10.1175/JAS-D-16-0296.1>
- Large, W. G., McWilliams, J. C., & Doney, S. C. (1994). Oceanic vertical mixing: A review and a model with a nonlocal boundary layer parameterization. *Reviews of Geophysics*, 32(4), 363–403. <https://doi.org/10.1029/94RG01872>
- Li, Q., Reichl, B. G., Fox-Kemper, B., Adcroft, A. J., Belcher, S. E., Danabasoglu, G., et al. (2019). Comparing ocean surface boundary vertical mixing schemes including Langmuir turbulence. *Journal of Advances in Modeling Earth Systems*, 11(11), 3545–3592. <https://doi.org/10.1029/2019MS001810>
- Lilly, D. K. (1962). On the numerical simulation of buoyant convection. *Tellus A: Dynamic Meteorology and Oceanography*, 14(2), 148–172. <https://doi.org/10.3402/tellusa.v14i2.9537>
- Marchesiello, P., Benshila, R., Almar, R., Uchiyama, Y., McWilliams, J. C., & Shchepetkin, A. (2015). On tridimensional rip current modeling. *Ocean Modelling*, 96, 36–48. <https://doi.org/10.1016/j.ocemod.2015.07.003>
- Mazzaro, L. J., Muñoz-Esparza, D., Lundquist, J. K., & Linn, R. R. (2017). Nested mesoscale-to-LES modeling of the atmospheric boundary layer in the presence of under-resolved convective structures. *Journal of Advances in Modeling Earth Systems*, 9(4), 1795–1810. <https://doi.org/10.1002/2017MS000912>
- McWilliams, J. C., Restrepo, J. M., & Lane, E. M. (2004). An asymptotic theory for the interaction of waves and currents in coastal waters. *Journal of Fluid Mechanics*, 511, 135–178. <https://doi.org/10.1017/S0022112004009358>
- McWilliams, J. C., Sullivan, P. P., & Moeng, C.-H. (1997). Langmuir turbulence in the ocean. *Journal of Fluid Mechanics*, 334, 1–30. <https://doi.org/10.1017/S0022112096004375>
- Mirocha, J., Kirkil, G., Bou-Zeid, E., Chow, F. K., & Kosović, B. (2013). Transition and equilibration of neutral atmospheric boundary layer flow in one-way nested large-eddy simulations using the weather research and forecasting model. *Monthly Weather Review*, 141(3), 918–940. <https://doi.org/10.1175/MWR-D-11-00263.1>
- Pope, S. B. (2000). Large-eddy simulation. In *Turbulent flows* (pp. 558–640). Cambridge University Press. <https://doi.org/10.1017/CBO9780511840531>
- Pressel, K. G., Mishra, S., Schneider, T., Kaul, C. M., & Tan, Z. (2017). Numerics and subgrid-scale modeling in large eddy simulations of stratocumulus clouds. *Journal of Advances in Modeling Earth Systems*, 9(2), 1342–1365. <https://doi.org/10.1002/2016MS000778>
- Scotti, A. (2010). Large eddy simulation in the ocean. *International Journal of Computational Fluid Dynamics*, 24(10), 393–406. <https://doi.org/10.1080/10618562.2010.522527>
- Silvestri, S., Wagner, G. L., Campin, J.-M., Constantinou, N. C., Hill, C. N., Souza, A. N., & Ferrari, R. (2024). A new WENO-based momentum advection scheme for simulations of ocean mesoscale turbulence. <https://doi.org/10.22541/essoar.170110657.76489860/v2>
- Skamarock, W. C. (2004). Evaluating mesoscale NWP models using kinetic energy Spectra. *Monthly Weather Review*, 132(12), 3019–3032. <https://doi.org/10.1175/MWR2830.1>
- Smolarkiewicz, P. K., Margolin, L. G., & Wyszogrodzki, A. A. (2007). Implicit large-eddy simulation in meteorology: From boundary layers to climate. *Journal of Fluids Engineering*, 129(12), 1533–1539. <https://doi.org/10.1115/1.2801678>
- Soufflet, Y., Marchesiello, P., Lemarié, F., Jouanno, J., Capet, X., Debreu, L., & Benshila, R. (2016). On effective resolution in ocean models. *Ocean Modelling*, 98, 36–50. <https://doi.org/10.1016/j.ocemod.2015.12.004>

- Souza, A. N., Wagner, G. L., Ramadhan, A., Allen, B., Churavy, V., Schloss, J., et al. (2020). Uncertainty quantification of ocean parameterizations: Application to the K-Profile-Parameterization for penetrative convection. *Journal of Advances in Modeling Earth Systems*, 12(12), e2020MS002108. <https://doi.org/10.1029/2020MS002108>
- Spalart, P. R. (2009). Detached-Eddy simulation. *Annual Review of Fluid Mechanics*, 41(1), 181–202. <https://doi.org/10.1146/annurev.fluid.010908.165130>
- Sutherland, G., Marié, L., Reverdin, G., Christensen, K. H., Broström, G., & Ward, B. (2016). Enhanced turbulence associated with the diurnal jet in the ocean surface boundary layer. *Journal of Physical Oceanography*, 46(10), 3051–3067. <https://doi.org/10.1175/JPO-D-15-0172.1>
- Taylor, J. R., & Thompson, A. F. (2023). Submesoscale dynamics in the upper Ocean. *Annual Review of Fluid Mechanics*, 55(1), 103–127. <https://doi.org/10.1146/annurev-fluid-031422-095147>
- Uchiyama, Y., McWilliams, J. C., & Shchepetkin, A. F. (2010). Wave-current interaction in an oceanic circulation model with a vortex-force formalism: Application to the surf zone. *Ocean Modelling*, 34(1), 16–35. <https://doi.org/10.1016/j.ocemod.2010.04.002>
- Umlauf, L., & Burchard, H. (2003). A generic length-scale equation for geophysical turbulence models. *Journal of Marine Research*, 61(2), 235–265. <https://doi.org/10.1357/002224003322005087>
- Umlauf, L., & Burchard, H. (2005). Second-order turbulence closure models for geophysical boundary layers. A review of recent work. *Continental Shelf Research*, 25(7), 795–827. <https://doi.org/10.1016/j.csr.2004.08.004>
- Umlauf, L., Smyth, W. D., & Moum, J. N. (2015). Energetics of bottom Ekman layers during buoyancy arrest. *Journal of Physical Oceanography*, 45(12), 3099–3117. <https://doi.org/10.1175/JPO-D-15-0041.1>
- Wagner, G. L., Hillier, A., Constantinou, N. C., Silvestri, S., Souza, A., Burns, K. J., et al. (2025). Formulation and calibration of CATKE, a one-equation parameterization for microscale Ocean mixing. *Journal of Advances in Modeling Earth Systems*, 17(4), e2024MS004522. <https://doi.org/10.1029/2024MS004522>
- Wenegrat, J. O., & McPhaden, M. J. (2015). Dynamics of the surface layer diurnal cycle in the equatorial Atlantic Ocean (0° , 23°W). *Journal of Geophysical Research: Oceans*, 120(1), 563–581. <https://doi.org/10.1002/2014JC010504>
- Wenegrat, J. O., & Thomas, L. N. (2020). Centrifugal and symmetric instability during Ekman adjustment of the bottom boundary layer. *Journal of Physical Oceanography*, 50(6), 1793–1812. <https://doi.org/10.1175/JPO-D-20-0027.1>
- Wyngaard, J. C. (2004). Toward numerical modeling in the “Terra Incognita”. *Journal of the Atmospheric Sciences*, 61(14), 1816–1826. [https://doi.org/10.1175/1520-0469\(2004\)061\(1816:TNTMITT\)2.0.CO;2](https://doi.org/10.1175/1520-0469(2004)061(1816:TNTMITT)2.0.CO;2)
- Zheng, Z., Wenegrat, J. O., Fox-Kemper, B., & Brett, G. J. (2025). Wind-Catalyzed energy exchanges between fronts and boundary layer turbulence. *Journal of Physical Oceanography*, 1(aop), 1591–1606. <https://doi.org/10.1175/JPO-D-24-0243.1>
- Zhou, B., Simon, J. S., & Chow, F. K. (2014). The convective boundary layer in the Terra Incognita. *Journal of the Atmospheric Sciences*, 71(7), 2545–2563. <https://doi.org/10.1175/JAS-D-13-0356.1>

References From the Supporting Information

- Khani, S. (2018). Mixing efficiency in large-eddy simulations of stratified turbulence. *Journal of Fluid Mechanics*, 849, 373–394. <https://doi.org/10.1017/jfm.2018.417>
- Sullivan, P. P., & McWilliams, J. C. (2018). Frontogenesis and frontal arrest of a dense filament in the oceanic surface boundary layer. *Journal of Fluid Mechanics*, 837, 341–380. <https://doi.org/10.1017/jfm.2017.833>
- Sullivan, P. P., & McWilliams, J. C. (2019). Langmuir turbulence and filament frontogenesis in the oceanic surface boundary layer. *Journal of Fluid Mechanics*, 879, 512–553. <https://doi.org/10.1017/jfm.2019.655>
- Sullivan, P. P., & McWilliams, J. C. (2024). Oceanic frontal turbulence. *Journal of Physical Oceanography*, 54(2), 333–358. <https://doi.org/10.1175/JPO-D-23-0033.1>